Chromatography and Anti-Biofilm Activity of Chiral Carbon Nanoparticles

by

Misché A. Hubbard

A dissertation submitted in partial fulfillment
of the requirements for the degree of
Doctor of Philosophy
(Chemical Engineering)
in the University of Michigan
2023

Doctoral Committee:

Professor Nicholas Kotov, Co-Chair
Associate Professor J. Scott VanEpps Co-Chair
Professor Angela Violi
Associate Professor Fei Wen

Misché A. Hubbard

mische@umich.edu

ORCID iD: 0000-0003-3993-8226

Dedication

To my grandparents, whose love, compassion, and perseverance motivated me every day of this journey. Your resilience made me the woman I am today.

Acknowledgements

I would like to thank my advisor, Prof. Nicholas Kotov, for giving me the honor to work in this extraordinary lab. I had no funding, no previous papers, but you saw something in me that I didn't see in myself. You never doubted me. Not a single day. You motivated and pushed me to live up to my potential. You always listened to my input and allowed me to chase my aspirations. I hope that you find your investment in me worth it. If I had the opportunity to do this again, I would choose you every time. I couldn't ask for a better advisor.

I'd like to thank my other advisor, Prof. J. Scott VanEpps, who accepted me as a student before even meeting me. Working on such an interdisciplinary project requires having multiple mentors. Thank you for mentoring me through uncharted waters and guiding me to success. Our meetings were always fun, enlightening, and gave me the power to conduct great research.

I would like to thank all Kotov members, both past and present. Drew, Connor, Elizabeth, Prashant, Ahmet, Sumeyra, Doug, Naomi, Jun, Harrison, Michal, Wenbing, Chung-Man, Yanan, Jinchen, Kody, Jessica, Alain and many more. You always gave me something to look forward to every day of lab. Our doorway discussions and conversations at Rappourt will always be some of the best memories I have from Kotov Lab. I could never have a bad day in lab with all of you by my side.

I'd like to thank VanEpps lab members as well: Erika, Shamalee, Chris, John, Shannon, Clemence, Joanne. You accepted me into the lab and always made sure I was doing well. You

helped me conduct experiments, write protocols, and provided daily giggles! Working with you all was so fun. I look forward to see where our friendship goes.

I can't forget all my friends outside of lab: Sean, Zach, Alex, Jacques, Patrick, Danielle, Rachael, Emily, Harrison, Anna, Jordyn, Marshall, Tobias, Ray, Connor, Z and Katey. You all provided so much adventure to my life here in Ann Arbor. From Friday hangouts at bills, to camping in the UP, kayaking down the Huron, or being tourists in Toronto, we always had so much fun. Thank you for giving me a life outside of lab.

Most importantly, I'd like to thank my family for supporting my academic journey. On my hardest and darkest days, you all reminded me I was more than capable and in exactly the right spot that I'm supposed to be. While I looked forward, you always had my back. I'm very grateful for all of your love and support.

Table of Contents

List of Tables

List of Figures

List of Appendices

Abstract

Biofilms have evolved to be resistant to natural and man-made antibiotics. The biochemical composition and barrier function of the extracellular polymeric substance prevent penetration of traditional antimicrobials reduce proliferation of bacterial cells embedded in it. Design of the agents capable of dispersing the biofilm matrix is obscured by its heterogeneity and variability. Here we seek to explore chiral nanoparticles as means to enantioselectively disperse amyloid rich biofilms. The first scope of this work is synthesize and characterize chiral nanoparticles, namely chiral carbon nanoparticles as a new class of anti-biofilm agents. Chiral carbon nanoparticles (CNPs) represent a rapidly evolving area of research for optical and biomedical applications. Similar to small molecules, further development of chiral chemistry of CNPs and fundamental understanding of the structural origin of their optical activity would greatly benefit from their enantioselective separations using established methods of chromatography with chiral stationary phases. However, this technique remains in its infancy for chiral CNPs and the possibility of such separations using high performance liquid chromatography (HPLC) remains an open question. In **Chapter 2**, we report a detailed methodology of HPLC for successful separation of chiral CNPs and establish a path for its future optimization. A mobile phase of water/acetonitrile was able to achieve chiral separation of CNPs derived from *L*- and *D*-cysteine denoted as *L*-CNPs and *D*-CNPs. Molecular dynamics simulations show that the teicoplanin-based stationary phase has a higher affinity for *L*-CNPs than for *D*-CNPs, in agreement with experiments. The experimental and computational findings jointly indicate that chiral centers of chiral CNPs are present at their

surface, which is essential for the multiple applications of these chiral nanostructures and equally essential for interactions with biomolecules and circularly polarized photons. In C**hapter 3**, we show that cysteine-derived chiral carbon nanoparticles (C^3NPs) are capable to disperse established amyloid-rich *Staphylococcus (S. aureus)* biofilms and reveal three modes of function-relevant biological interaction. We found that C^3NPs from *D*-cysteine (*D*-C^3NPs) are much more efficient in biofilm dispersal than those from *L*-cysteine (*L*-C^3NPs). Unlike small molecules, the cooperativity of the intermolecular interactions leads to strong binding between C^3NPs and phenol soluble modulins (PSM), the monomeric form of amyloid fibers within the biofilm. First, the formation of PSMα1 nanofibers known as the essential structural component of the extracellular polymeric substance was prevented by both *D*- and *L*-C^3NPs due the strong change in their assembly patterns leading to formation of rigid nanotubes disrupting the co-assembly with other biofilm components. Second, *D*- but not *L*-C^3NPs distort conformation and thus prevent fibrillation of PSMα3 peptide known for nucleating assembly of other nanofibers. Molecular dynamics simulations confirm chirality-dependent interactions of C^3NPs with amino acid residues essential for PSM self-assembly. Third, agglutination of both types of PSMs promoted by NPs prevented their dispersal as virulence factors as confirmed by cytotoxicity data that including hemolysis rate and cytokine production. Subsequent engineering of molecular and nanoscale chirality of C^3NPs will enable their further adaptation to the biomedical needs and clinical requirements.

Chapter 1 Introduction

1.1 Biofilms

1.1.1 What are Biofilms?

Biofilms are surface attached communities of microorganisms encased in a self-generated extracellular polymer substance (EPS). Besides planktonic cells, the EPS contains a heterogeneous arrangement of exopolymers including polysaccharides, eDNA, lipids, and proteins. These three-dimensional structures form on abiotic or biotic surfaces and can be found in the environment, industrial systems, and hospital settings. Biofilms are essential for Earth's biodiversity and overall sustainability of life. For example, soil beneficial biofilms support plan development through enhanced nutrient accessibility, organic compound mineralization, and the release of phytohormones.[1] Beneficial biofilms are employed during wastewater treatment to remove contaminants and compounds such as nitrogen and phosphorous.[2] Furthermore, biofilms in the gastrointestinal system facilitate communication between intestinal microbes and host via microbial compounds such as metabolites, cell components, and other small molecules.[3] While biofilms are crucial in various situations, they can also be quite detrimental. Biofouling occurs when biofilms created by micro-organisms accumulate on surfaces with mechanical functions and causes structural damage or other deficiencies. Biofouling in pipes causes a reduction in flow rates, increased pressure drops, and corrosion.[4] In aquatic settings, biofilms are known to attach to ship hulls, offshore structures, and underwater surfaces. This fouling causes increased drag which reduces fuel efficiency while increasing greenhouse gas emission and maintenance costs.[5,6] It is estimated that between 65%-80% of nosocomial infections are related to bacterial biofilms.[7,8]

These encompass both device-related and non-device-related infections.[8] Compared to free floating planktonic cells, bacterial cells within biofilms can be up to 1000 more resistant to conventional anti-biotics.[9] The increased resistance can be attributed to the protective EPS which acts as a barrier and prevents diffusion of antibiotics into the biofilm. Furthermore, bacteria within biofilms have altered physiological characteristics such as reduced metabolic activity and altered gene expression, making the bacteria less susceptible to antibiotics that target essential cellular processes.[10] Biofilm bacteria also employ efflux pumps to actively expel antimicrobial agents, reducing the intracellular concentration and lowering the efficacy of these molecules. The combination of these resistance factors contribute to the resilience of biofilms, necessitating alternative approaches to increase the efficacy of antimicrobial agents.

1.1.2 Current Anti-Biofilm Agents

The advent of synthesized antibiotics revolutionized healthcare and is one of greatest achievements of therapeutic medicine. Alexander Fleming discovered penicillin in the late 1920's which is regarded as the drug that began the era of antibiotics. [11] The synthesis and production of penicillin played a critical war in World War II. Prior to this, there were greater casualties from infectious disease compared to enemy gunfire.[11] In 1945, the public gained access to penicillin, breaking its exclusivity as a military medication and dramatically improved patient outcomes of millions.[12] Other novel antibiotics were discovered between the 1940's and 1960's called the "golden age of antibiotics".[11,13,14] Many of the antibiotics discovered during this period are still in clinical use today. Typical mechanisms of actions for these drugs are to interfere with vital mechanisms or components within the bacterial cell. Selective pressure from antibiotics coupled with overuse and misuse exacerbated the rise of multi-drug resistance bacteria. Analogs of antibiotics were synthesized by modifying the chemical structure to bypass resistance

mechanisms.[15] While this strategy worked for short periods of time, structural similarities to existing antibiotics increased the likelihood of resistance development. Because of the analog based discovery approach, there have only been two new classes of antibiotic marketed since this period since the 1960's.[16] The rise of resistant pathogens is outpacing the discovery of antimicrobials.[14] Furthermore, antibiotics are designed to target planktonic cells and not the biofilms. It's imperative to design new chemotherapeutics to disperse and eliminate biofilms.

Currently, there are no drugs approved by the Food and Drug Administration (FDA) to treat biofilm related infections.[17] As result, researchers are actively searching for novel compounds specifically for biofilms. There are many strategies currently under investigation to treat biofilm related infections. For example, antimicrobial peptides (AMPs) hold promise as potential antimicrobial agents. These small peptides are between 10-60 amino acids with hydrophobic and cationic residues to interact with bacterial membranes and degrade the biofilm matrix components.[17] There are several challenges and limitations to using AMPs such as high synthesis and production costs, susceptibility to proteolytic decay, and they have narrow spectrum activity which restricts they applicability for treating polymicrobial infections or diverse biofilm populations.[18–20] Small molecules are being explored to inhibit quorum sensing systems, a communication mechanism between bacteria to sense and adjust their phenotype based on environmental conditions.[21] Quorum sensing inhibitors (QSIs) disrupt biofilms by interfering with the production or reception of autoinducers, which disrupts coordination and cooperation of bacteria within the biofilm. Some limitations of QSIs include lack of specificity, disruption of healthy microbiota, and the protective EPS layer prevents penetration reducing their overall efficacy. Various EPS degrading strategies are also being explored for their anti-biofilm activity. EPS degrading enzymes, antibodies, and nucleic acids have shown to disturb the matrix and reduce

adherence to surfaces, cell-to-cell adhesion and aggregation.[22] Similar to AMPs, EPS degrading molecules are susceptible to degradation and have limited shelf life.[23] Furthermore, lack of specificity may have adverse effects to host tissues or other off targeted areas.[23] While the strategies listed show some promise as new classes of antibiotics, these methods present selective pressures indicating that biofilms can adapt and develop resistance mechanisms over time. New classes of anti-biofilm agents should have high stability and specificity, and not present selective pressures to minimize resistance mechanism development.

1.2 Chiral Nanomaterials

1.2.1 Inorganic Nanomaterials

Inorganic nanoparticles are materials ranging from 1 to 100 nm in at least one dimension and have unique physicochemical properties in comparison bulk materials of the same composition. A key feature of nanomaterials is their high surface area to volume ratio which allows for facile surface functionalization and increases their chemical reactivity.[24] Common types of nanomaterials include but are not limited to nanoparticles, nanotubes, nanowires, nanofibers, and quantum dots. The versatile nature of nanoparticles presents research opportunities across a broad spectrum of disciplines including photonics, electronics, catalysis, and biomedical applications.

1.2.2 Chiral Inorganic Nanoparticles

Chirality is a geometrical property of objects or molecules that lack symmetry and cannot be superimposable onto its mirror image. Objects with mirror images are called enantiomers and have distinct handedness: left-handed (levorotary or "*L*-") and right handed (dextrorotary or "*D*-"). Chirality plays an important role in the fields of chemistry, biology, pharmacology, and material science. In biology, homochirality refers to a phenomena where one enantiomer dominates while

the other is less abundant or absent.[25] For example, naturally occurring amino acids are in the "*L*" conformation while sugars are in the "*D*" configuration. Homochirality has a profound effect on biology activity and function of molecules.[26] Specifically, enantiomers of drugs can exhibit different pharmacological effects with one enantiomer being effective while the other may be inactive or even exhibit adverse effects.[27]

Chirality in inorganic nanostructures can arise from their specific crystal structure, surface chemistry, or arrangement of atoms or ligands. Chiral inorganic nanoparticles have the traditional advantages of nanoparticles and unique properties that arise from their asymmetric structure. The ability to induce strong circular dichroism (CD) and circular polarized luminescence (CPL) responses coupled with enhanced chiral effects at the nanoscale make chiral nanoparticles favorable for asymmetric catalysis[28], chiral sensing[29], drug delivery[30], chiral chromatography[31], and photonics[32].

1.2.3 Chiral Carbon Nanoparticles

Carbon nanoparticles (CNPs) are 0-dimensional, quasispherical semiconductor nanoparticles typically less than 10 nm.[33] CNPs are typically composed of graphitic or turbostratic sp^2 hybridized carbon.[34] They can also contain oxygen, sulfur, nitrogen depending on the dopants and reactants used during synthesis. CNPs have attracted much interest because of their light emissive properties and low toxicity compared to traditional semiconductor nanoparticles such as cadmium or lead.[34] Because of their size and composition, these carbon-based nanomaterials exhibit interesting optical, electronic, and chemical properties.[35]

Researchers have recently been investigating the effects of incorporating chirality with carbon nanoparticles. The focus has been tailored towards discovering synthesis routes and applications of chiral CNPs (cCNPs). Current applications of chiral CNPs include light emitting devices[36],

chiral catalysis[37], and bio-applications such as mimicking enzymes[38]. The size and shape of cCNPs enable them to be ideal materials for interacting with other nanoscale biomolecules (proteins, peptides, polysaccharides, DNA). cCNPs have proven to enantioselectively modulate the morphology and functions of biomolecules. For example, *D*-cysteine derived CNPs (D-CNPs) were more effective at catalyzing the transition of DNA from supercoiled to open-circular configuration compared to *L*-CNPs.[38] Chiral CNPs can also act as enzyme nanohybrids where *L*-CNPs significantly enhance the activity of glucose oxidase and improve its delivery to cancer cells compared to the other enantiomer.[39] In another example, *L*-lysine derived CNPs removed the secondary structure and fibril morphologies of Aβ42 while D-CNPs displayed minimal effects.[40] Interestingly, chiral CNPs have also been explored for their antimicrobial activity. *D*-cysteine derived CNPs displayed higher anti-bacterial properties against *Escherichia coli* (*E.coli*) at lower concentrations than *L*-CNPs.[41] Antibacterial activity of chiral CNPs has also been reported for other microorganisms as well but their anti-biofilm activity has yet to be explored.[42] chiral CNPs offer a promising new class of antibiofilm agents based on their ability to target planktonic bacteria and to enantioselectively interact with biomolecules similar to those located within the EPS.

1.3 Research Goals

In this work, I explore the anti-biofilm activity of cysteine derived chiral carbon nanoparticles (C^3NPs) in the following manner:

1. Synthesis and characterization of C^3NPs with multiple scales of chirality
2. Display enantioselective display of pathogenic biofilms
3. Determine the mechanism of action for biofilm disassembly.

1.4 Chapter Summaries

1.4.1 Chapter 2: Synthesis and Characterization of Cysteine Derived Chiral Carbon Nanoparticles

There are many ways to synthesize chiral CNPs using top-down or bottom-up approaches, but the origin of chirality is still not well understood. In this chapter, we use cysteine as the source of chirality and the carbon precursor and use a hydrothermal synthesis to carbonize the amino acid into nanoparticles. Then we use an array of techniques, including chromatography, to determine where the chiral centers are located within the particle. This work highlights novel methods for identifying, purifying, an understanding the stability of cCNPs.

1.4.2 Chapter 3: Antibiofilm Activity of Cysteine Derived Chiral Carbon Nanoparticles

This chapter highlights the anti-biofilm activity of cysteine derived cCNPs against pathogenic *Staphyloccocus aureus (S.aureus)*. The antibiofilm efficacy of CNPs is assessed against static and flow cell biofilms. Modulation of biofilm components by cCNPs, namely amyloid peptides, is also explored. Molecular dynamics simulations are also included to confirm and explain the phenomenon found experimentally.

1.4.3 Chapter 4: Conclusions and Future Work

This chapter summarizes the key findings in **Chapter 2** and **Chapter 3** and how they can be optimized to advance the use of chiral carbon nanoparticles as anti-biofilm agents. Chiral CNPs made from other starting materials and comments on how testing these nanoparticles on *S. aureus* and other pathogens such as *E.coli* and *Pseudomonas aeruginosa* are also included.

1.5 References

1. Rossi, F. Beneficial biofilms for land rehabilitation and fertilization. *FEMS Microbiology Letters* **367**, fnaa184 (2020).
2. Ünal Turhan, E., Erginkaya, Z., Korukluoğlu, M. & Konuray, G. Beneficial biofilm applications in food and agricultural industry. *Health and safety aspects of food processing technologies* 445–469 (2019).
3. Sommer, F. & Bäckhed, F. The gut microbiota—masters of host development and physiology. *Nature reviews microbiology* **11**, 227–238 (2013).
4. Bixler, G. D. & Bhushan, B. Biofouling: lessons from nature. *Philosophical Transactions of the Royal Society A: Mathematical, Physical and Engineering Sciences* **370**, 2381–2417 (2012).
5. De Carvalho, C. C. C. R. Marine biofilms: a successful microbial strategy with economic implications. *Frontiers in marine science* **5**, 126 (2018).
6. Georgiades, E., Scianni, C. & Tamburri, M. N. Biofilms associated with ship submerged surfaces: implications for ship biofouling management and the environment. *Frontiers in Marine Science* **10**, 1197366 (2023).
7. Lewis, K. I. M. Riddle of biofilm resistance. *Antimicrobial agents and chemotherapy* **45**, 999–1007 (2001).
8. Jamal, M. *et al.* Bacterial biofilm and associated infections. *Journal of the Chinese Medical Association* **81**, 7–11 (2018).
9. Ceri, H. *et al.* The Calgary Biofilm Device: new technology for rapid determination of antibiotic susceptibilities of bacterial biofilms. *Journal of clinical microbiology* **37**, 1771–1776 (1999).

10. Mah, T.-F. C. & O'Toole, G. A. Mechanisms of biofilm resistance to antimicrobial agents. *Trends in microbiology* **9**, 34–39 (2001).

11. Mohr, K. I. History of Antibiotics Research BT - How to Overcome the Antibiotic Crisis : Facts, Challenges, Technologies and Future Perspectives. in (eds. Stadler, M. & Dersch, P.) 237–272 (Springer International Publishing, 2016). doi:10.1007/82_2016_499.

12. Nicolaou, K. C. & Rigol, S. A brief history of antibiotics and select advances in their synthesis. *The Journal of Antibiotics* **71**, 153–184 (2018).

13. Ribeiro da Cunha, B., Fonseca, L. P. & Calado, C. R. C. Antibiotic Discovery: Where Have We Come from, Where Do We Go? *Antibiotics* vol. 8 Preprint at https://doi.org/10.3390/antibiotics8020045 (2019).

14. Aminov, R. I. A brief history of the antibiotic era: lessons learned and challenges for the future. *Frontiers in microbiology* **1**, 134 (2010).

15. Spratt, B. G. Resistance to Antibiotics Mediated by Target Alterations. *Science* **264**, 388–393 (1994).

16. Coates, A. R. M., Halls, G. & Hu, Y. Novel classes of antibiotics or more of the same? *British Journal of Pharmacology* **163**, 184–194 (2011).

17. van Tilburg Bernardes, E., Lewenza, S. & Reckseidler-Zenteno, S. Current research approaches to target biofilm infections. *Postdoc journal: a journal of postdoctoral research and postdoctoral affairs* **3**, 36 (2015).

18. Hancock, R. E. W. & Lehrer, R. Cationic peptides: A new source of antibiotics. *Trends in Biotechnology* vol. 16 82–88 (1998).

19. Lei, J. *et al.* The antimicrobial peptides and their potential clinical applications. *American Journal of Translational Research* **11**, 3919 (2019).

20. Andersson, D. I., Hughes, D. & Kubicek-Sutherland, J. Z. Mechanisms and consequences of bacterial resistance to antimicrobial peptides. *Drug Resistance Updates* **26**, 43–57 (2016).

21. Shi, Y. *et al.* Exploiting extracellular polymeric substances (EPS) controlling strategies for performance enhancement of biological wastewater treatments: An overview. *Chemosphere* vol. 180 396–411 (2017).

22. Koo, H., Allan, R. N., Howlin, R. P., Stoodley, P. & Hall-Stoodley, L. Targeting microbial biofilms: Current and prospective therapeutic strategies. *Nature Reviews Microbiology* vol. 15 740–755 (2017).

23. Jiang, Y., Geng, M. & Bai, L. Targeting biofilms therapy: Current research strategies and development hurdles. *Microorganisms* **8**, 1222 (2020).

24. Khalid, K. *et al.* Advanced in developmental organic and inorganic nanomaterial: A review. *Bioengineered* **11**, 328–355 (2020).

25. Sallembien, Q., Bouteiller, L., Crassous, J. & Raynal, M. Possible chemical and physical scenarios towards biological homochirality. *Chem Soc Rev* **51**, 3436–3476 (2022).

26. Blackmond, D. G. The origin of biological homochirality. *Cold Spring Harb Perspect Biol* **2**, a002147 (2010).

27. McConathy, J. & Owens, M. J. Stereochemistry in drug action. *Prim Care Companion J Clin Psychiatry* **5**, 70 (2003).

28. Hao, C. *et al.* Chiral Semiconductor Nanoparticles for Protein Catalysis and Profiling. *Angewandte Chemie* **131**, 7449–7452 (2019).

29. Huang, Y., Nguyen, M. K., Natarajan, A. K., Nguyen, V. H. & Kuzyk, A. A DNA Origami-Based Chiral Plasmonic Sensing Device. *ACS Applied Materials and Interfaces* **10**, 44221–44225 (2018).

30. Chen, X. *et al.* Chiral Nanosilica Drug Delivery Systems Stereoselectively Interacted with the Intestinal Mucosa to Improve the Oral Adsorption of Insoluble Drugs. *ACS Nano* **17**, 3705–3722 (2023).

31. Shukla, N., Bartel, M. A. & Gellman, A. J. Enantioselective Separation on Chiral Au Nanoparticles. *Journal of the American Chemical Society* **132**, 8575–8580 (2010).

32. Kumar, P. *et al.* Photonically active bowtie nanoassemblies with chirality continuum. *Nature* **615**, 418–424 (2023).

33. Ying Lim, S., Shen, W. & Gao, Z. Carbon quantum dots and their applications. *This journal is Cite this: Chem. Soc. Rev* **44**, 362 (2015).

34. Ying Lim, S., Shen, W. & Gao, Z. Carbon quantum dots and their applications. *This journal is Cite this: Chem. Soc. Rev* **44**, 362 (2015).

35. Đorđević, L. *et al.* Design principles of chiral carbon nanodots help convey chirality from molecular to nanoscale level. doi:10.1038/s41467-018-05561-2.

36. Zhang, Z. *et al.* One-step microwave preparation of carbon dots-composited G-quartet hydrogels with controllable chirality and circularly polarized luminescence. *Carbon* **203**, 39–46 (2023).

37. Bartolomei, B., Corti, V. & Prato, M. Chiral Carbon Nanodots Can Act as Molecular Catalysts in Chemical and Photochemical Reactions. *Angewandte Chemie* (2023)

38. Li, F. *et al.* Chiral Carbon Dots Mimicking Topoisomerase I To Mediate the Topological Rearrangement of Supercoiled DNA Enantioselectively. *Angewandte Chemie International Edition* **59**, 11087–11092 (2020).

39. Gao, P. *et al.* Chiral Carbon Dots-Enzyme Nanoreactors with Enhanced Catalytic Activity for Cancer Therapy. *ACS Applied Materials and Interfaces* **13**, 56456–56464 (2021).

40. Malishev, R. *et al.* Chiral modulation of amyloid beta fibrillation and cytotoxicity by enantiomeric carbon dots. *Chemical Communications* **54**, 7762–7765 (2018).

41. Victoria, F., Manioudakis, J., Zaroubi, L., Findlay, B. & Naccache, R. Tuning residual chirality in carbon dots with anti-microbial properties. *RSC Advances* **10**, 32202–32210 (2020).

42. Zhao, D. *et al.* The preparation of chiral carbon dots and the study on their antibacterial abilities. *Materials Chemistry and Physics* **295**, 127144 (2023).

Chapter 2 Chiral Chromatography and Surface Chirality of Carbon Nanoparticles

This chapter was adapted from: Hubbard, MA, Luyet, C, Kumar, P, et al. Chiral chromatography and surface chirality of carbon nanoparticles. *Chirality*. 2022; 34(12): 1494- 1502.

2.1 Introduction

Carbon nanoparticles (CNPs) have attracted extensive research interest for their unique physicochemical properties.[2–4] CNPs with an average diameter of <10 nm share the desirable optical and electronic properties of typical semiconductor quantum dots while avoiding disadvantages such as intrinsic toxicity from the use of heavy metals, harsh synthesis conditions, and expensive starting materials.[5–7] CNPs and other nanocarbons display strong photoluminescence, easy functionalization, exceptional biocompatibility, high stability, and chemical inertness, making them useful for an array of applications including light emitting diodes[8], biosensors[9], photocatalysts[10], bioimaging[11], and drug delivery[12].

Mirror asymmetric CNPs with multiple scales of chirality from molecular to nanoscale, have the advantages of achiral CNPs with the added capability of chiral recognition for multitude of biochemical, biomedical, and sustainability applications. *L*- and *D*-CNPs elicit distinctly different supramolecular interactions with biological molecules based on their handedness. For example, *L*-lysine CNPs remodeled the secondary structure of amyloid-β (aβ-42) peptides and inhibited key factors of pathogenesis, including cytolysis and amyloid fibril fibrillation, while *D*-lysine CNPs displayed little to no biological activity against the same peptide.[13] Cysteine-derived *L*-CNPs upregulated glycolysis within human bladder cancer T24 cells while *D*-CNPs did not display similar effects.[14] Chiral CNPs synthesized from cysteine electrostatically interact with porphyrins

to form supramolecular porphyrins–CNP hybrids, where the chirality of the CNPs transfers to the porphyrins and the CD signal are enhanced.[15] Apart from graphene quantum dots[16], the localization of chiral centers within the CNPs remains an open question. CNPs were reported to have predominantly spherical geometries but could potentially have chiral geometries at multiple scales. Among those, CNPs are hypothesized to have the tetrahedral coordinated carbon centers inherited from chiral precursors but it is not clear whether these molecular structures can survive the high temperature carbonization processes used for their preparation. Additionally, CNPs may also display nanoscale chirality associated both with ligand distribution at the interface and twist-distortions in the CNP interior.[17] All of these structural features will result in a chiral environment around chromophores that will generate optical activity.[18–20]

The potential use of chiral CNPs for applications in biology, medicine, catalysis and optics motivates us to determine whether the chiral centers in CNPs are located in the interior or at the interface of the particles. Importantly, the same question emerges when one needs to find reproducible methods for separating enantiomeric NPs. High performance liquid chromatography (HPLC) is the gold-standard method for chiral separations but has not been extended to resolving chiral nanoparticle solutions. Solution gradients are widely used for HPLC to separate analytes with disparate chemical composition. Chiral separations are typically conducted in isocratic conditions, making the mobile phase essential for separation yet difficult to optimize.[21] Here, chiral resolution of cysteine-derived chiral CNPs was achieved using a simple water/ acetonitrile mobile phase. To the best of our knowledge, this is the first report on enantioselective HPLC for the separation of enantiomeric NPs. The chiral stationary phase (CSP) employs the macrocyclic glycopeptide teicoplanin as the chiral selector grafted to silica gel via linkage chains, and has been ideal for separating un-derivatized amino acids and other polar ionic chiral compounds.[22–24]

Molecular dynamics simulations show that *D*-CNPs preferentially interact with teicoplanin compared to *L*-CNPs, which is in agreement with the longer retention time of *D*-CNPs found experimentally. Chiral HPLC analysis of chiral nanostructures can determine enantiomeric nanoparticle purity and provide new methods for chiral separation and isolation. Simultaneously, these findings indicate that the surface of CNPs contains chiral centers.

2.2 Experimental Section

2.2.1 Materials.

CNP precursors, namely *L*-cysteine (*L*-cys) or *D*-cysteine (*D*-cys) and sodium hydroxide (NaOH) were purchased from Millipore Sigma. Racemic mixture of the amino acid cysteine (*rac*-cys), was prepared by mixing equal volumes of solution of *L*-cys and *D*-cys with a concentration of 1 mg/mL. Dialysis tubes with molecular weight cut off 1 kDa was obtained from Fischer Scientific. Acetonitrile (HPLC grade) was purchased from Millipore Sigma. All solutions were prepared using ultrapure water (18.2 MΩ·cm).

2.2.2 Synthesis of L- or D-CNPs.

Chiral CNPs were synthesized asymmetrically by a hydrothermal method as previously described.[25] 0.5 g of *L*-cys or *D*-cys and 1g of NaOH was dissolved in 10 mL of water under ultrasonification for 20 minutes. The prepared solution was transferred into a 25 mL Teflon lined autoclave and heated at 120 °C for 16hr. The mixture was dialyzed to remove unreacted material for 3 days. The final product was filtered against a 0.22 micron filter to remove large aggregates and then lyophilized for storage. Optically pure *L*- and *D*-CNPs were re-suspended to a final concentration of 1 mg/mL in ultrapure water prior to HPLC analysis.

2.2.3 Circular Dichroism.

CD spectra were acquired in a Jasco-815 spectrophotometer. The spectra were recorded from 190 nm to 500 nm, at 1 nm intervals, 1 nm bandwidth, and a scan speed of 100 nm/min.

2.2.4 Vibrational Circular Dichroism.

VCD measurements were performed on CNP samples dispersed in heavy water (D_2O) at a concentration of 33 mg/ml. A 100 µl drop was sandwiched between two BaF_2 crystals separated by 50 µm Teflon spacer. MCT-V detector was used to acquire IR and VCD data in the range 1800-850 cm^{-1} with a resolution of 4 cm^{-1} and a total of 200 and 1000 accumulations, respectively. The sandwiched dispersion between BaF_2 crystals was rotated along an axis coinciding with the direction of the beam at a constant speed to avoid settling of particles. Corresponding IR and VCD were plotted as absorbance (A) and differential absorbance of left- and right- circularly polarized light (ΔA) respectively with exclusion of 1300 to 1100 cm^{-1} range that corresponds to strong absorption from D_2O.

2.2.5 Chiral HPLC Analysis.

Chiral CNPs were separated using an Agilent 6000 Series LC/MS instrument with an Astec CHIROBIOTIC T 10 cm x 4.6 mm (Millipore Sigma) chiral column. The mobile phase consisted of ultrapure water and acetonitrile (30:70 v/v) applied over 10 minutes at a flow rate of 1 mL min^{-1}. UV detection was set to 205 nm.

2.2.6 Molecular Dynamics.

The affinity of *L*- and *D*-CNPs with teicoplanin was computed with biased all-atom simulations. The CHARMM force field, version 36, was employed and the systems were solvated using explicit TIP3P water.[26,27] First, systems were minimized and equilibrated in the isothermal-isobaric ensemble for at least 150 ns, where a Langevin piston Nose-Hoover method (with a period of 200

fs and 50 fs decay) maintained a pressure of 100 kPa. A Langevin thermostat (with a characteristic time of 20 ps) was used to keep the temperature constant. A time step of 2 fs was employed to integrate the equations of motion, and hydrogen atoms are kept rigid via the SHAKE algorithm. Non-bonded short-range interactions smoothly approached 0 using an X-PLOR switching function between 1 and 1.2 nm, in conjunction with the particle mesh Ewald algorithm to evaluate long-range Coulombic forces. Nanoscale Molecular Dynamics (NAMD) software was used for running the simulations.[28]

Free energy surfaces were reconstructed using well-tempered Metadynamics simulations in the canonical ensemble over the course of 630 ns or more.[29,30] Gaussian-shaped bias (σ = 0.04 nm, initial height 0.2 kcal/mol) was deposited with pace 0.4 ps, and scaled using a bias factor of 10. Simulations were biased on the distance between teicoplanin's center of mass (COM) and the COM of each chiral CNP (d_{COM}). A harmonic wall was placed at 5 nm. The free energy was calculated as the time average difference between the bound state (distance <= 2.5 nm) and the unbound state (distance $\geq$ 3 nm). PLUMED 2 was used for all simulation.[31,32] Visual Molecular Dynamics (VMD) was used for data visualization, and the MDAnalysis and Matplotlib Python libraries were used for visualization and data analysis.[33–36]

2.3 Results and Discussion

Reversed-phase HPLC is the most common method for chiral analysis of amino acids and protein fragments. Analysis of protein fragments is achieved by chemical or enzymatic hydrolysis of proteins, followed by HPLC separation and, finally, analysis on mass spectrometry to identify protein sequence[37]. Chiral CNPs are similar in size (2-10 nm) and molecular weight (10^3-10^5 g/mol) to proteins, yet if their chiral moieties are located on the surface, hydrolysis will be unnecessary for chiral analysis.[38] Furthermore, biological molecules, namely proteins, are known

to adsorb onto the surface of CNPs changing the physicochemical properties of the NPs[39]. Chiral HPLC analysis can be employed to characterize protein coronas by analyzing changes in retention time, which suggests changes in polarity or chirality in the case of CNP induced racemization. This makes chiral HPLC analysis a powerful tool to understand enantiomeric interactions between biological molecules and chiral CNPs.

Chiral CNPs were synthesized using a hydrothermal route using cysteine as both the carbon and chiral precursor[40], **Fig. 2.1a**. Synthesis conditions (temperature and duration) were the same for synthesizing *L*-CNPs and *D*-CNPs to ensure their physicochemical properties were similar (size distribution, crystal structure, surface functionalization). Subsequent characterization indicated that *L*-CNPs and *D*-CNPs have similar chemical structure and properties with exception of mirror symmetric relations between some chemical structures constituting the near-spherical particles. The main body of this manuscript will focus on the characterization of *L*-CNPs. More information on the physical and chemical properties of *D*-CNPs can be found in **Appendix A**.

Morphological characteristics of the chiral CNPs were obtained using transmission electron microscopy (TEM) images that reveal both *L*- and *D*-CNPs have a size distribution between 2-7 nm (**Fig. 2.1b**) which may be expected to be a challenge in their characterization and separation by chromatography. Scanning transmission electron microscopy high-angle annular dark field images (STEM-HAADF) images in **Fig. 2.1c** confirm the size distribution and morphology of

NPs as seen in TEM images.

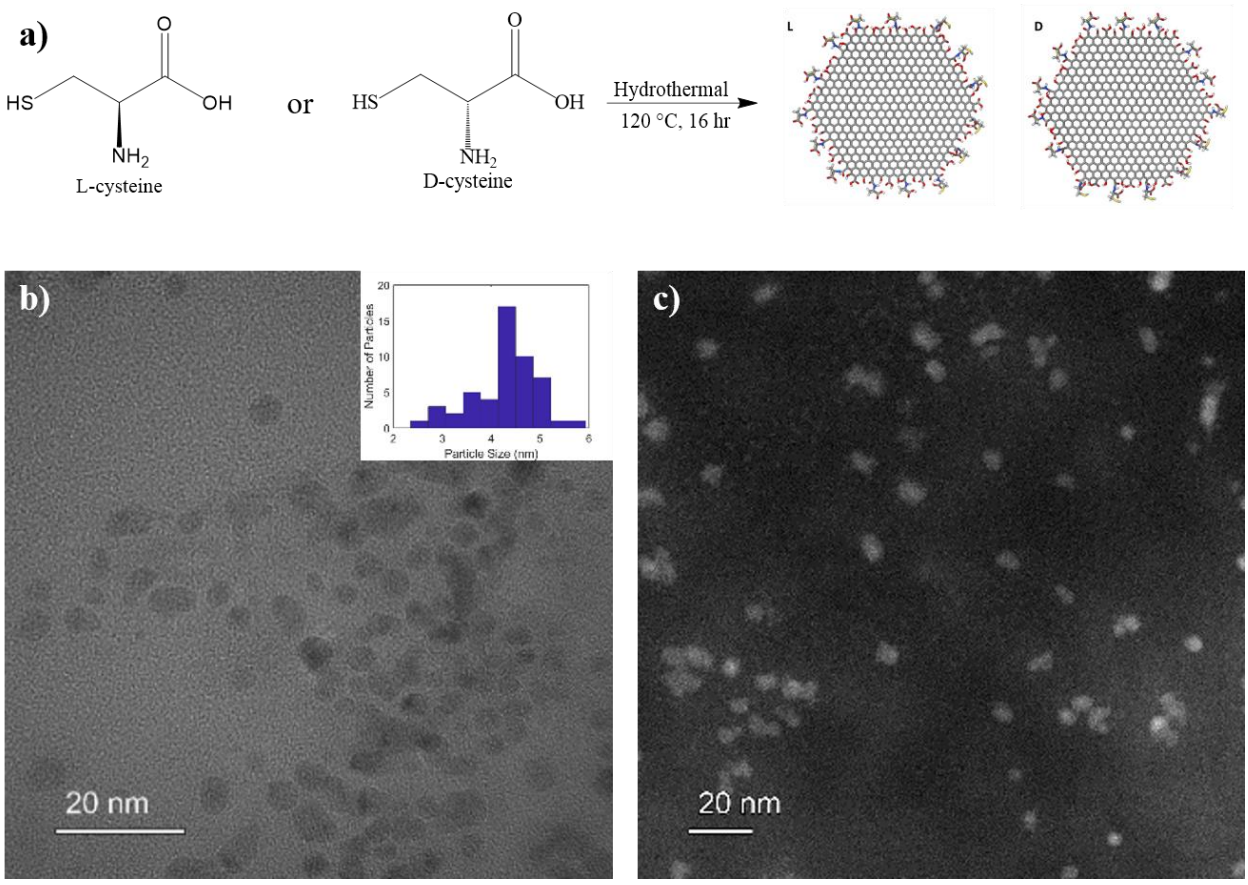

Figure 2.1: a) Schematic of chiral CNP synthesis b) TEM of *L*-CNPs with histogram inlay. c) STEM image of *L*-CNPs.

The zeta potential (ζ) of chiral CNPs was measured to determine the surface charge (A.1). At pH 7, chiral CNPs display a strong negative charge of –27 ± 0.66 mV and –28.7 ± 0.26 mV for *L*-CNPs and *D*-CNPs, respectively. The negative charge is consistent with the presence of carboxyl groups at the edges.

The optical properties of chiral CNPs were observed using UV-vis spectroscopy. For both *L*- and *D*-CNPs, two peaks were seen at 200 nm and 280 nm, which are attributed to the π-π* transition of the sp^2 hybridized carbon network (**Fig. 2.2a**).[16] Fourier Transform Infrared Spectroscopy (FT-IR) was employed to determine the functional groups conjugated to the surface of the chiral CNPs (**Fig. 2.2b**). The broad absorption band between 3200-3600 cm^{-1} are attributed to –OH and –NH

stretching vibrations. The peak at 2970 cm^{-1} indicates C-H bonds. The vibrational signals near 1750 cm^{-1} and 1620 cm^{-1} were attributed to C=O and C=C, respectively.[41] The presence of C-S bonds was seen by the absorption band at 1195 cm^{-1}. FT-IR spectra confirmed the presence of carboxyl, amino, and thiol groups at the surface of the chiral CNPs.

The photoluminescence spectra of chiral CNPs show the maximum emission wavelength between at ~475 nm after 365 nm excitation (**Fig. 2.2c, 2.2d**). They indicate that the CNPs have typical light emission of conjugated aromatic compounds. The luminescence properties of these NPs are convenient for both analysis and biomedical applications.

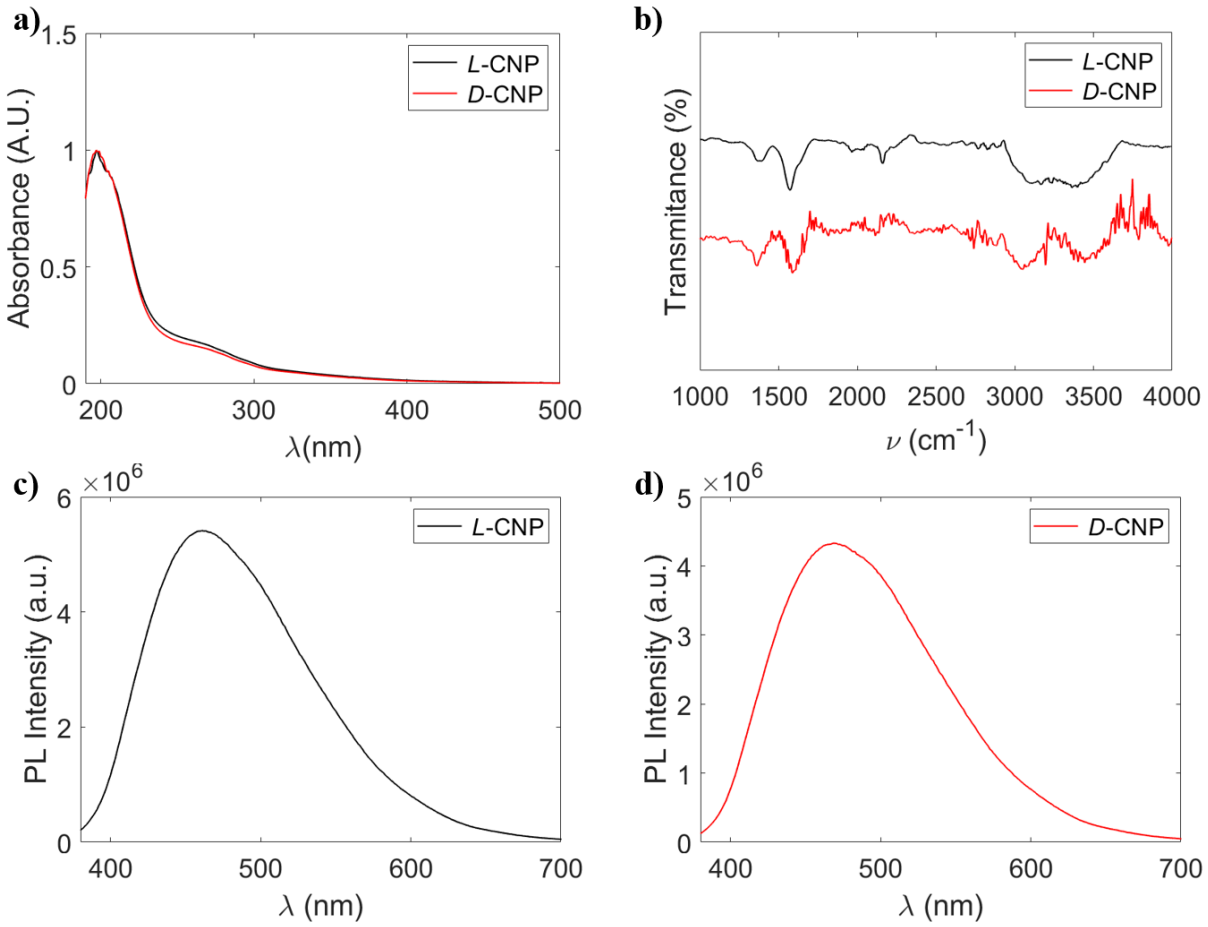

Figure 2.2: a) UV-vis spectra of chiral CNPs b) FT-IR spectra of chiral CNPs c) PL spectrum of *L*-CNPs d) PL spectrum of *D*-CNPs.

Circular dichroism (CD) spectroscopy was used to investigate the chiroptical properties of the CNPs. CD spectra of *L*- and *D*- CNPs in **Fig. 2.3a** reveal symmetrical and opposite high-energy peaks at 205 nm which is the chiral signal from cysteine molecules. Both *L*- and *D*-CNPs gave rise to a new symmetrical CD signal at around 260 nm, which suggests there's an interaction between cysteine and the graphitic core of the CNPs.[42]

IR and vibrational circular dichroism (VCD) spectra were acquired to determine conformational information about heavy water solutions of chiral CNPs. VCD data from previous reports of enantiomeric cysteine show mirror symmetry at the 1621 cm^{-1} peak.[43] The mirror symmetric opposite band at 1600 cm^{-1} in **Fig. 2.3b** indicates that the chirality is transferred from the cysteine molecules to the CNPs. The IR spectrum in **Fig. 2.3c** shows an antisymmetric stretching vibration at 1600 cm^{-1} of carboxyl groups, which agrees which FT-IR data found in **Fig 2.2c**. Owing to the organic nature of CNPs the VCD spectra is on the order of 10^{-4}.

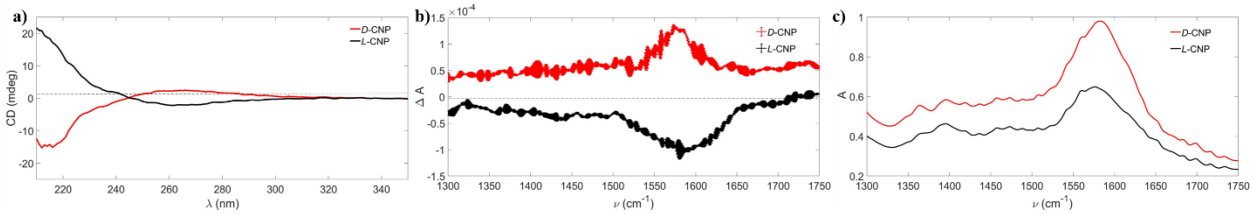

Figure 2.3: a) CD spectra b) VCD spectra and c) IR spectra of chiral CNPs.

The retention times of *rac*-cys and chiral CNPs can be found in **Table 2.1.** For *rac*-cys and chiral CNPs, the *D*- enantiomer had longer retention times compared to the *L*-enantiomer, which matches previous reports in literature.[24] *rac*-cys contained two retention times, where *L*-cys resolved at 3.305 ± 0.145 mins and *D*-cys shortly after at 3.368 ± 0.017 mins.

Table 2.1: Retention Times of rac-cys and chiral CNPs after separation on CHIROBIOTIC T column for HPLC

Analyte	**Retention Time 1 (min)**	**Retention Time 2 (min)**
rac-cys	3.305 ± 0.145	3.368 ± 0.017
L-CNP	0.795 ± 0.046	-
D-CNP	0.961 ± 0.022	-

Fig. 2.4a shows the corresponding chromatogram for *rac*-cys separation. The chiral CNPs eluted much faster than their cysteine precursors at 0.795 ± 0.046 mins and 0.961 ± 0.022 mins for *L*-and *D*- CNPs, respectively (**Fig. 2.4b**). The longer retention times of the CNPs indicates their size prevents them interacting with chiral bonding sites deep within the CSP. This suggests that chiral ligands at the surface of the CNPs are the primary mechanism for enantioselective separation through polar ionic interactions.

The resolution quality may be improved by adding organic or alcohol modifiers to the mobile phase. Reducing the polarity of the solvent will lower the elution strength and allow more π-π interactions between the chiral CNPs and the CSP. The size distribution of the chiral CNPs may also allow individual particles to have non-uniform interactions along the column. Further purification and fractionation of the CNPs can lower the size distribution and may improve enantioselective separation.

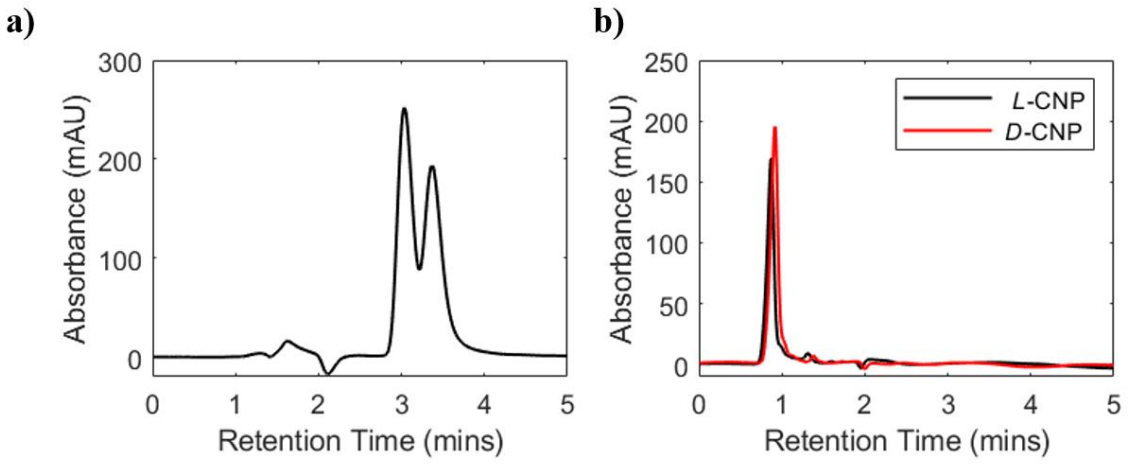

Figure 2.4: Chromatograms of a) rac-cys and b) chiral CNPs separated on an Astec CHIROBIOTIC T column for HPLC.

Chiral CNPs were captured after separation to ensure they maintain their morphology and physicochemical properties. UV-vis spectroscopy found in **Fig. 2.5a** shows two similar peaks at 200 nm and 260 nm as seen in **Fig. 2.2** indicating minimal changes to the crystal structure of the CNPs. This point is confirmed by emission spectra of eluted CNPs. After 365 nm excitation, the same high-energy peak can be found between 450 – 500 nm similar to that in **Fig. 2.2**. TEM microscopy of eluted CNPs maintain their size distribution of indicating the column separates by chirality and not by size. TEM also highlight the CNPs retain the lamellar structure of graphene which proves CNPs are highly stable and resistant to hydrolysis. The stability of CNPs after separation allows the nanoparticles to be fractionated using HPLC for analysis or to be used in future experiments.

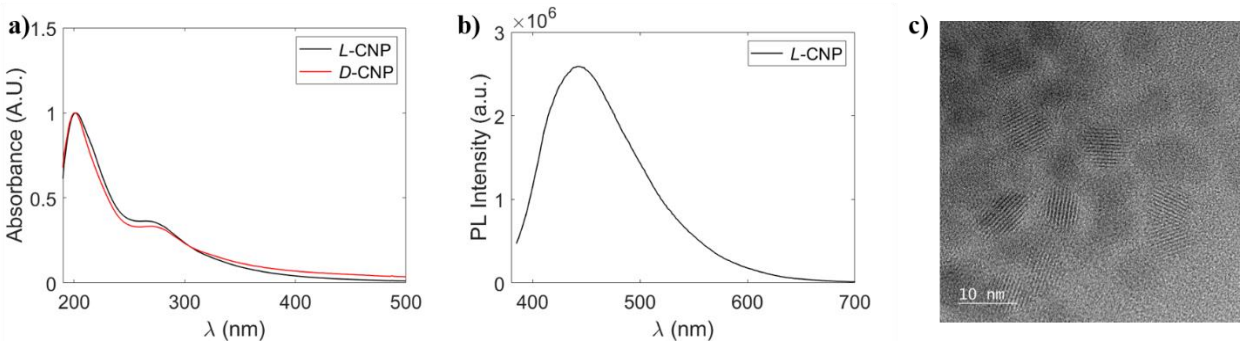

Figure 2.5: a) UV-vis spectra b) Emission spectrum c) TEM image of *L*-CNPs following chiral separation.

It has been established that teicoplanin is bound to aminopropyl silica gel through a bifunctional aliphatic isocyanate.[44] Nonetheless, an incomplete understanding of the covalent grafting makes *in silico* investigation more difficult.[45] Consequently, unbound teicoplanin was used to study its interaction with chiral CNPs using biased molecular dynamics (MD) simulations. Two simplified models were generated, one for teicoplanin with chiral NPs made from two cysteine enantiomers, under the mobile phase conditions stated above, to mimic the chromatographic conditions. Metadynamics simulations reveal a binding free energy for teicoplanin with *L*-and *D*-CNPs to be 0.35 ± 0.51 and -1.95 ± 0.64, respectively (**Table 2.2**), where the error is standard deviation.

Table 2.2: Binding free energy of teicoplanin and chiral CNPs.

System	**Δ*A* (kcal/mol)**	**Standard Deviation**
L-CNP	0.35	0.51
D-CNP	-1.95	0.64

The higher binding energy for the teicoplanin/*L*-CNP system suggests a weaker or unfavorable interaction. Interestingly, *L*-CNPs become warped in close proximity to teicoplanin (**Fig. 2.6a**); furthermore, the center of mass distance between teicoplanin's binding region and the *L*-CNP ($d_{binding}$) tends to be larger than for the *D*-CNP when they are interacting. For example, teicoplanin's binding region orients itself closer to the *D*-CNP in **Fig. 2.6d**, a possible rationalization for the difference in affinity (**Tab. 2)**. Overall, MD simulations highlight the higher binding affinity between teicoplanin and *D*-CNPs, confirming the elution order found in experiments. This suggests MD simulations can be powerful tools for understanding the interactions of chiral NPs and chiral selectors.[46,47] Furthermore, MD simulations can be employed to screen multiple parameters to find suitable conditions for enhanced resolution between enantiomers.

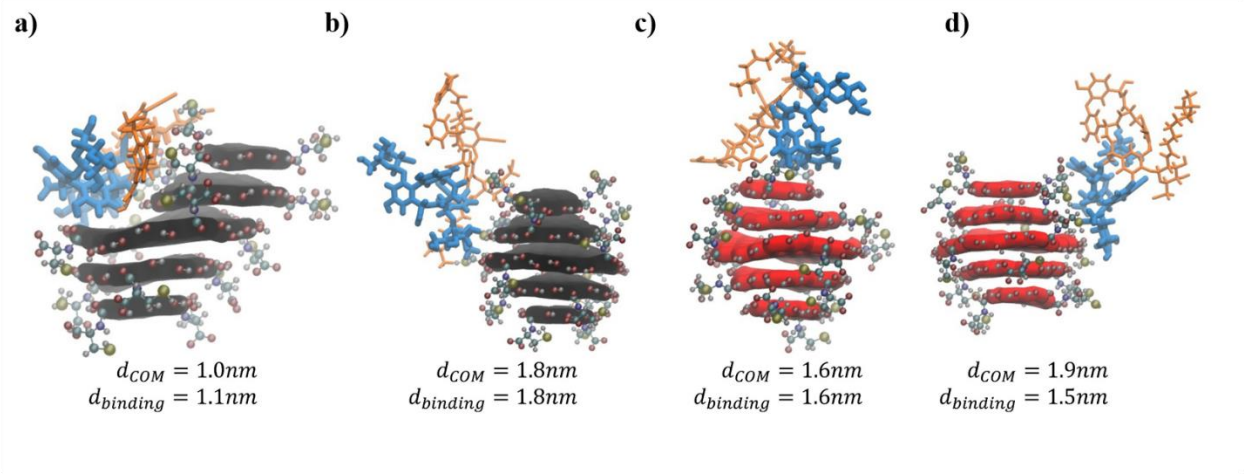

Figure 2.6: Chiral CNPs interacting with teicoplanin segments on the HPLC column. Teicoplanin (orange and blue), teicoplanin binding region (blue), *D*-CNP (red), and *L*-CNP (black).

2.4 Conclusions

Chiral CNPs made from two enantiomeric forms of cysteine were successfully separated using a water/acetonitrile mobile phase on an Astec CHIROBIOTIC T chiral column, which indicates the

presence of chiral centers located on their surface. Besides the analytical importance enabling further development of biomedical and other applications of chiral nanoparticles, this finding is essential for the accurate physical picture of their interactions with cellular membranes[48] and biomacromolecules[49]. Various mirror asymmetric structures may also exist in the NP interior exemplified by the twist of their crystalline nanoparticle interior, helical conformation of molecular components, and a mirror-asymmetric surface. Unlike semiconductor and metal NPs[50,51], the presence of these non-local components of multiscale chirality for CNPs remains uncertain. Furthermore, the condensation reactions leading to CNP formation are likely to lead to randomization and racemization of substituents around sp^3 carbons. The ability of HPLC columns with teicoplanin stationary phase to separate these *L*- and *D*-CNPs give strong indication that *L*- and *D*-centers of cysteine are retained. Additionally, these data indicate that chiral CNPs are hydrolytically stable and resist degradation into their precursor cysteine. The dominating forces behind chiral separations were steric hindrance and polar ionic. MD simulations were employed to investigate the interaction between chiral NPs and the chiral selector. This technique provides a new method for detecting and quantifying chiral NPs. While providing foundation for future chiral HPLC analysis of chiral NPs, chiral HPLC analysis of NPs can also provide an analytical toolbox for future studies of chiral recognition mechanisms and methods for interacting with different chiral centers.

2.5 References

1. Hao, C. *et al.* Chiral Semiconductor Nanoparticles for Protein Catalysis and Profiling. *Angew. Chemie* **131**, 7449–7452 (2019).
2. Ragazzon, G. *et al.* Optical processes in carbon nanocolloids. *Chem* **7**, 606–628 (2021).
3. Kang, Z. & Lee, S. T. Carbon dots: advances in nanocarbon applications. *Nanoscale* **11**,

19214–19224 (2019).

4. Rod, K. A. *et al.* Water-dispersible nanocolloids and higher temperatures promote the release of carbon from riparian soil. *Vadose Zo. J.* **19**, e20077 (2020).
5. Chen, F. *et al.* Graphene quantum dots in biomedical applications: Recent advances and future challenges. *Front. Lab. Med.* **1**, 192–199 (2017).
6. Zhang, N. *et al.* Quantum-dots-based photoelectrochemical bioanalysis highlighted with recent examples. *Biosens. Bioelectron.* **94**, 207–218 (2017).
7. Li, L. & Yan, X. Colloidal Graphene Quantum Dots. *J. Phys. Chem. Lett.* **1**, 2572–2576 (2010).
8. Kumar, G. S., Thupakula, U., Sarkar, P. K. & Acharya, S. Easy extraction of water-soluble graphene quantum dots for light emitting diodes. *RSC Adv.* **5**, 27711–27716 (2015).
9. Xu Wu *et al.* Fabrication of highly fluorescent graphene quantum dots using l-glutamic acid for in vitro / in vivo imaging and sensing. *J. Mater. Chem. C* **1**, 4676–4684 (2013).
10. Zeng, Z., Chen, S., Tan, T. T. Y. & Xiao, F. X. Graphene quantum dots (GQDs) and its derivatives for multifarious photocatalysis and photoelectrocatalysis. *Catal. Today* **315**, 171–183 (2018).
11. Chung, S., Revia, R. A. & Zhang, M. Graphene Quantum Dots and Their Applications in Bioimaging, Biosensing, and Therapy. *Adv. Mater.* **33**, 1904362 (2021).
12. Iannazzo, D. *et al.* Graphene quantum dots for cancer targeted drug delivery. *Int. J. Pharm.* **518**, 185–192 (2017).
13. Malishev, R. *et al.* Chiral modulation of amyloid beta fibrillation and cytotoxicity by enantiomeric carbon dots. *Chem. Commun.* **54**, 7762–7765 (2018).

14. Li, F. *et al.* Highly Fluorescent Chiral N-S-Doped Carbon Dots from Cysteine: Affecting Cellular Energy Metabolism. *Angew. Chemie* **130**, 2401–2406 (2018).

15. Liu, X. *et al.* Chiral Self-Assembly of Porphyrins Induced by Chiral Carbon Dots. *Front. Chem.* **8**, 670 (2020).

16. Suzuki, N. *et al.* Chiral Graphene Quantum Dots. *ACS Nano* **10**, 1744–1755 (2016).

17. Visheratina, A., Kumar, P. & Kotov, N. Engineering of inorganic nanostructures with hierarchy of chiral geometries at multiple scales. *AIChE J.* **68**, e17438 (2022).

18. Tedesco, D. & Bertucci, C. Induced circular dichroism as a tool to investigate the binding of drugs to carrier proteins: Classic approaches and new trends. *J. Pharm. Biomed. Anal.* **113**, 34–42 (2015).

19. Döring, A., Ushakova, E. & Rogach, A. L. Chiral carbon dots: synthesis, optical properties, and emerging applications. *Light Sci. Appl. 2022 111* **11**, 1–23 (2022).

20. Wei, Y. *et al.* Investigation on the chirality mechanism of chiral carbon quantum dots derived from tryptophan †. (2019).

21. Pirok, B. W. J., Gargano, A. F. G. & Schoenmakers, P. J. Optimizing separations in online comprehensive two-dimensional liquid chromatography. *J. Sep. Sci.* **41**, 68 (2018).

22. Aboul-Enein, H. Y. & Ali, I. Chiral resolution of cromakalim by HPLC on teicoplanin and teicoplanin aglycon chiral stationary phases. *Journal of Liquid Chromatography and Related Technologies* **25**, 2337–2344 (2002).

23. Berthod, A. Chiral recognition mechanisms with macrocyclic glycopeptide selectors. *Chirality* **21**, 167–175 (2009).

24. Claus, J. E. Chiral HPLC Analysis of Underivatized Amino Acid Enantiomers. *Reporter* **29**, 8–9 (2011).

25. Hu, L. *et al.* Nitrogen and sulfur co-doped chiral carbon quantum dots with independent photoluminescence and chirality. *Inorg. Chem. Front.* **4**, 946–953 (2017).

26. Huang, J. & Mackerell, A. D. CHARMM36 all-atom additive protein force field: Validation based on comparison to NMR data. *J. Comput. Chem.* **34**, 2135–2145 (2013).

27. Jorgensen, W. L., Chandrasekhar, J., Madura, J. D., Impey, R. W. & Klein, M. L. Comparison of simple potential functions for simulating liquid water. *J. Chem. Phys.* **79**, 926 (1998).

28. Phillips, J. C. *et al.* Scalable molecular dynamics with NAMD. *J. Comput. Chem.* **26**, 1781–1802 (2005).

29. Barducci, A., Bonomi, M. & Parrinello, M. Metadynamics. *Wiley Interdiscip. Rev. Comput. Mol. Sci.* **1**, 826–843 (2011).

30. Barducci, A., Bussi, G. & Parrinello, M. Well-tempered metadynamics: A smoothly converging and tunable free-energy method. *Phys. Rev. Lett.* **100**, 020603 (2008).

31. Bonomi, M. *et al.* PLUMED: A portable plugin for free-energy calculations with molecular dynamics ☆. *Comput. Phys. Commun.* **180**, 1961–1972 (2009).

32. Tribello, G. A. *et al.* PLUMED 2: New feathers for an old bird. *Comput. Phys. Commun.* **185**, 604–613 (2014).

33. Michaud-Agrawal, N., Denning, E. J., Woolf, T. B. & Beckstein, O. MDAnalysis: A toolkit for the analysis of molecular dynamics simulations. *J. Comput. Chem.* **32**, 2319–2327 (2011).

34. Hunter, J. D. Matplotlib: A 2D Graphics Environment. *Comput. Sci. Eng.* **9**, 90–95 (2007).

35. Gowers, R. *et al.* MDAnalysis: A Python Package for the Rapid Analysis of Molecular

Dynamics Simulations. *Proc. 15th Python Sci. Conf.* 98–105 (2016).

36. Humphrey, W., Dalke, A. & Schulten, K. VMD: Visual molecular dynamics. *J. Mol. Graph.* **14**, 33–38 (1996).

37. Ali, I., Suhail, M. & Aboul-Enein, H. Y. Chiral analysis of macromolecules. *J. Liq. Chromatogr. Relat. Technol.* **41**, 749–760 (2018).

38. Wang, Y. *et al.* Anti-Biofilm Activity of Graphene Quantum Dots via Self-Assembly with Bacterial Amyloid Proteins. *ACS Nano* **13**, 4278–4289 (2019).

39. Huang, R., Carney, R. P., Stellacci, F. & Lau, B. L. T. Protein–nanoparticle interactions: the effects of surface compositional and structural heterogeneity are scale dependent. *Nanoscale* **5**, 6928 (2013).

40. Zhang, Y. & He, J. Facile synthesis of S, N co-doped carbon dots and investigation of their photoluminescence properties. *Phys. Chem. Chem. Phys.* **17**, 20154–20159 (2015).

41. Chen, C., Zhao, D., Hu, T., Sun, J. & Yang, X. Highly fluorescent nitrogen and sulfur co-doped graphene quantum dots for an inner filter effect-based cyanide sensor. *Sensors Actuators, B Chem.* **241**, 779–788 (2017).

42. Qu, D. *et al.* Highly luminescent S, N co-doped graphene quantum dots with broad visible absorption bands for visible light photocatalysts †. *Nanoscale* **5**, 12272–12277 (2013).

43. Kamiński, M., Kudelski, A. & Pecul, M. Vibrational optical activity of cysteine in aqueous solution: A comparison of theoretical and experimental spectra. *J. Phys. Chem. B* **116**, 4976–4990 (2012).

44. D'acquarica, I. *et al.* Direct chromatographic resolution of carnitine and O-acylcarnitine enantiomers on a teicoplanin-bonded chiral stationary phase. *J. Chromatogr. A* **857**, 145–

155 (1999).

45. Sardella, R., Ianni, F., Cossignani, L., Aldini, G. & Carotti, A. Binding modes identification through molecular dynamic simulations: A case study with carnosine enantiomers and the Teicoplanin A2-2-based chiral stationary phase. *J. Sep. Sci.* **43**, 1728–1736 (2020).

46. Elvati, P., Baumeister, E. & Violi, A. Graphene quantum dots: effect of size, composition and curvature on their assembly. *RSC Adv.* **7**, 17704–17710 (2017).

47. Elvati, P. & Violi, A. Free Energy Calculation of Permeant–Membrane Interactions Using Molecular Dynamics Simulations. *Methods Mol. Biol.* **926**, 189–202 (2012).

48. Ostadhossein, F., Vulugundam, G., Misra, S. K., Srivastava, I. & Pan, D. Chirality Inversion on the Carbon Dot Surface via Covalent Surface Conjugation of Cyclic α-Amino Acid Capping Agents. *Bioconjug. Chem.* **29**, 3913–3922 (2018).

49. Li, F. *et al.* Chiral Carbon Dots Mimicking Topoisomerase I To Mediate the Topological Rearrangement of Supercoiled DNA Enantioselectively. *Angew. Chemie Int. Ed.* **59**, 11087–11092 (2020).

50. Kumar, J., Thomas, A. K. G. & Liz-Marzá, L. M. Nanoscale chirality in metal and semiconductor nanoparticles. *Chem. Commun* **52**, 12555 (2016).

51. Xia, Y., Zhou, Y. & Tang, Z. Chiral inorganic nanoparticles: Origin, optical properties and bioapplications. *Nanoscale* **3**, 1374–1382 (2011).

Chapter 3 Anti-Biofilm Activity of Chiral Carbon Nanoparticles

This chapter is adapted from a manuscript currently in preparation: **Hubbard,MA.,** Luyet, C., Altheim,C., Baalbaki, N., Elvati, P., Violi, A.,VanEpps. J.S., Kotov, N., "Anti-biofilm Activity of Chiral Carbon Nanoparticles". *Manuscript in Preparation*

3.1 Introduction

Bacterial biofilms have been implicated in numerous illnesses and nosocomial infections[1]. Biofilm formation is a defense strategy imposed by bacteria to survive harsh environmental conditions, host immune responses, and conventional small molecule antibiotics.[2,3] The bacterial cells embedded within the biofilm are up to 1000 times more tolerant to antibiotics than free floating cells.[4,5] The decrease in antibiotic susceptibility can be attributed to the altered phenotype of biofilm cells embedded in a extracellular polymeric matrix (EPS), a protective biological composite from entangled polysaccharides, extracellular DNA (eDNA), lipids, and proteins,[6] which creates hard-to-penetrate barrier for nearly all antimicrobials capable of disrupting membrane or cellular machinery of bacterial cells.[7,8] Some antimicrobial peptides are capable to penetrate them by self-assembling with EPS and have shown broad-spectrum anti-biofilm activity.[9,10] However, peptides are expensive and difficult to manufacture at scale and have a short half-life that is further reduced by enzymes imbedded in the biofilm, which limits their use in a clinical setting.[11] Design of biomolecular agents specifically targeting the skeleton of the biofilm is obscured by the exceptional diversity of polymeric substances in EPS, which make targeting specific chemical biomolecules difficult. For example, EPS-degrading enzymes, such as glycoside hydrolases, DNases, and Dispersin B, target polysaccharides and DNA components in the EPS

and expose bacterial cells to the antibiotics.[12] However, they are, in turn, degraded by proteases within biofilms. Enzymes also require specific co-factors, pH, and salinity to function which may not be present in the microenvironment of an infection.[13]

Problems with current anti-biofilm strategies require the implementation of new antimicrobial agents. Carbon nanoparticles (CNPs) have been studied extensively for their tunable fluorescent properties, low toxicity, and excellent biocompatibility.[14–17] CNPs have already found applications in catalysis[18], biosensing[19], bioimaging[20], cancer therapy[21], and drug delivery.[22] They were also investigated for antibacterial activity against planktonic cultures of *Staphylococcus aureus* and *E. coli* due to generation of reactive oxygen species, membrane disruption, and self-assembly with intracellular proteins responsible for bacteria growth.[23,24] Chirality of NPs offers an opportunity to enhance their specificity. Thus, chiral CNPs (cCNPs) have been investigated for their biological applications, including antimicrobial activity. Taking advantage of chiral CNPs' tendency to self-assemble with biological macromolecules, we hypothesize chiral CNPs can interfere with the self-assembly process of biomolecules within the EPS, namely amyloid-like proteins, causing disruption. This hypothesis stems from multiple observations of CNPs asymmetric hierarchical self-assembly with amyloid peptides. Between CNPs made from *L*- or *D*-lysine, the particles from *L*-lysine had a high binding affinity and remodeled the secondary structure of amyloid beta – 42 (Aβ42) proteins while *D*-lysine CNPs seemed to have minimal effects.[25] In another study, both enantiomers of lysine CNPs acted as chiral amyloid inhibitors in the presence of lipid vesicles, but again *L*-lysine CNPs had a more pronounced effect on prion peptide fibrillation and morphology than *D*-lysine CNPs.[26] It can be anticipated that chiral CNPs will experience enantioselective interactions with EPS amyloid peptides and cause biofilm dispersal. It should be

noted that chiral CNPs are resistant to proteolytic decay and have a high molecular weight, which is an advantage over current anti-biofilm platforms.[27]

Here, were report the anti-biofilm activity of *L*- and *D*-cysteine derived chiral CNPs against amyloid-rich *S. aureus* biofilm, a major cause of healthcare associated infections worldwide.[28] The structuring and dispersion of *S. aureus* biofilms is dependent on bacterial excretion of phenol soluble modulins (PSMs), which are short alpha-helical, amphipathic peptides, and are critical determinants of *S. aureus* pathogenesis.[29,30] Self-assembly of PSM peptides into amyloid-like fibers is a key component of *S. aureus* biofilms, providing structural support and making physical or chemical dispersion of the biofilm very difficult. Both *L*- and *D*-CNPs are capable of dispersing *S. aureus* biofilms, yet *D*-CNPs demonstrated enhanced anti-biofilm activity highlighting the chiral recognition capabilities of the components within the EPS. Furthermore, chiral CNPs self-assemble with PSM peptides and modulate their morphology and biological activity based on the handedness of the nanoparticle. Molecular dynamics (MD) simulations were used to investigate the interactions of PSM peptides with chiral CNPs. Simulations confirm that chiral CNPs form long-lasting interactions with PSMs and modulate their secondary structure.

3.2 Results and Discussion

3.2.1 Chiral CNP Characterization

Chiral CNPs were synthesized from cysteine which acts as both the source of carbon and chiral precursor. To ensure the physical properties of the CNPs were similar, the reaction conditions were held constant. Because of the similarity between chiral CNPs, characterization for *L*-CNPs will be displayed primarily. More information regarding the characterization of *D*-CNPs can be found in **Appendix B.1**. TEM images indicate the *L*-CNPs have a size distribution from 2-7 nm (**Figure 3.1a**). In **Figure 3.1b**, UV-visible spectra of chiral CNPs contain peaks near 200 nm and 280 nm,

which can be attributed to the absorption of cysteine moieties and $\pi \rightarrow \pi^*$ of sp^2 hybridized carbons within the crystal lattice, respectively. Excitation dependent emission of *L*-CNPs can be seen in **Figure 3.1c**, with maximum emission of 400 nm after 320 nm excitation, which is typical for conjugated aromatic compounds. Fourier transform infrared spectroscopy (FT-IR) data of chiral CNPs is depicted in **Figure 3.1d**. Peaks near 1360 – 1400 cm^{-1}, 1600 cm^{-1} related to COO and C=C stretching vibrations respectively. Strong adsorption bands between 3200 cm^{-1} and 3600 cm^{-1} can be attributed to – OH and –NH stretching vibrations. FT-IR reveals hydroxyl, carboxyl, and amine groups located at the surface of chiral CNPs.

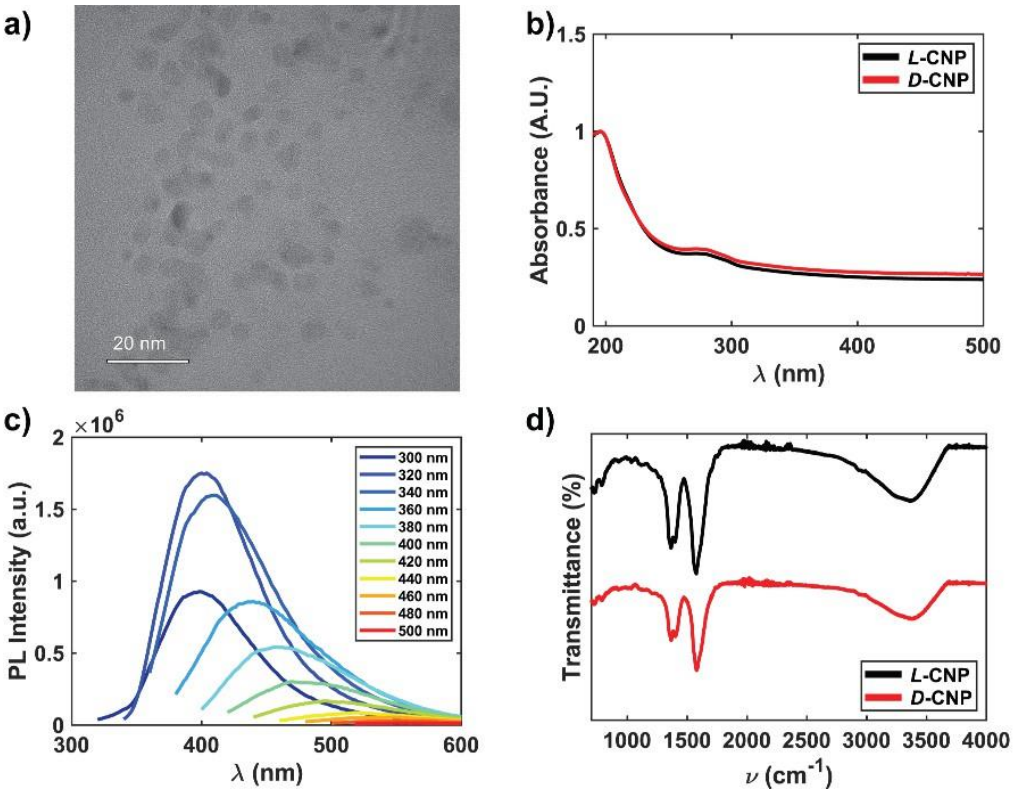

Figure 3.1: Structural and spectroscopic characterization of cCNPs. a) TEM images of *L*-CNPs b) UV-vis spectra of chiral CNPs c) Emission spectra of *L*-CNPs d) FT-IR spectra of cCNPs. Note the spectra are shifted on the y-axis to improve readability.

Chiroptical activity of chiral CNPs is displayed in Figure 2. CD spectra in **Figure 3.2a** reveal mirror high energy bands around 220 nm and a new peak around 260 nm suggesting there are

strong interactions between the cysteine molecules on the surface and the carbon core of the CNPs when the amino acid is attached to the carbon core *via* more than one bond and in more than one configuration.[31]. Enantiomeric cysteine elicits absorption at 1621 cm^{-1}.[32] Mirror symmetric bands can be seen near 1600 cm^{-1} in **Figure 3.2b** indicating chirality was successfully transferred from cysteine molecules to the CNPs.[31] The IR spectrum (**Figure 3.2c)** aligns well with FT-IR in **Figure 3.1** and highlights antisymmetric stretching vibrations are related to carboxyl groups. All of these spectra indicate molecular scale chirality of the CNP surface and its potential to enantioselectively interact with nanoscale biomolecules.

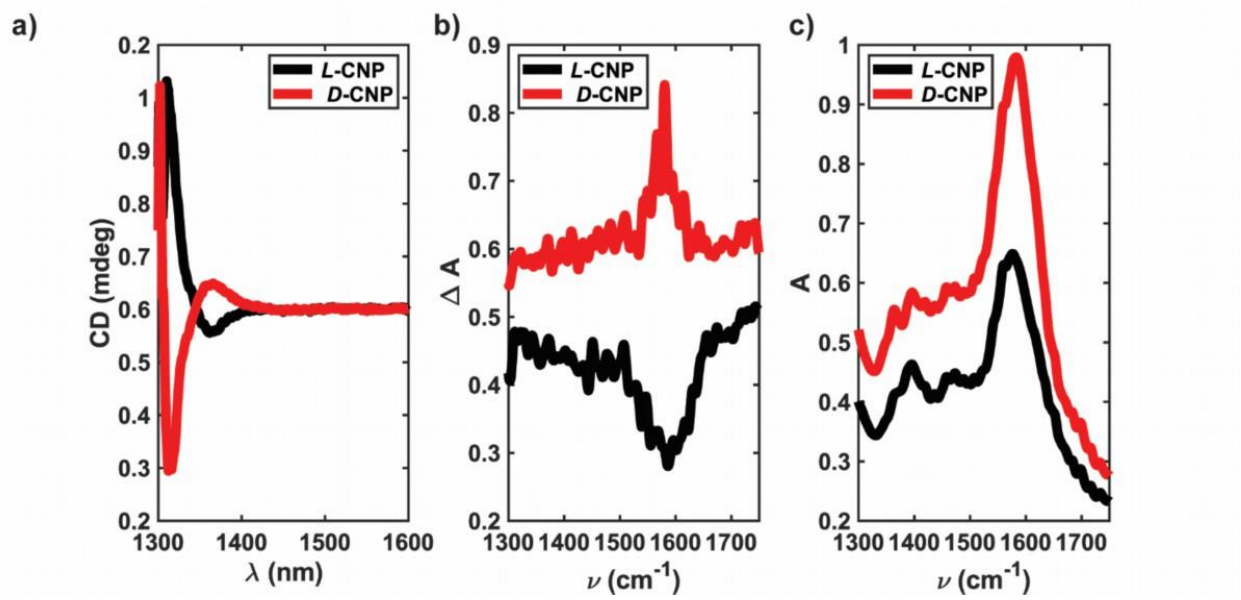

Figure 3.2 : Optical and chiroptical activity of chiral CNPs. a) CD b) VCD and c) IR spectra. Adapted with permission from Ref [31]© Chirality 2022.

3.2.2 Anti-Biofilm Activity of Chiral CNPs

Wang *et al.* previously established that achiral CNPs disperse amyloid rich staphylococcal biofilms at concentrations of 500 µg/mL and above,[27] which informed this study in respect to chiral CNPs dosage. To assess the effect of chiral CNPs on amyloid rich *S. aureus* biofilms, biofilms were grown statically at 37 °C for 24 hours and then, treated with either *L*- or *D*-CNPs at 1000 µg/mL,

500 µg/mL, or 50 µg/mL in peptone-NaCl-glucose (PNG) growth media, which promotes amyloid-rich biofilms. Scanning electron micrographs of untreated *S. aureus* biofilms show high surface area coverage and cell density (**Figure 3.3a**). The same biofilms treated with *L*-CNPs had a modest qualitative reduction in surface coverage and cell density (**Figure 3.3b**) while *D*-CNP treated biofilms had much greater reductions in surface coverage and cell density (**Figure 3.3c**). Biofilm dispersal was quantitatively assessed using a crystal violet (CV) assay. CV data confirms that both CNP enantiomers have anti-biofilm activity with *D*-CNPs eliciting higher dispersal effect compared to *L*-CNPs (**Figure 3.3d**). Chiral modulation of amyloid rich *S. aureus* biofilms was confirmed again using confocal microscopy images from biofilms grown in dynamic flow cell models. Here, biofilms were grown under flow conditions for 3 days before they were treated with 1000 µg/mL of chiral CNPs. Untreated, control biofilms displayed high surface coverage and cell density (**Figure 3.3e**). *L*-CNPs did reduce surface coverage of *S. aureus* (**Figure 3.3f**), but *D*-CNPs had a more robust reduction in surface coverage (**Figure 3.3g**). Quantitative image analysis shows that *L*- and *D*-CNPs reduced surface coverage from 43.3 ±3 .4% to 32.7 ± 6.6 % and 23.3 ± 6.8%, respectively (**Figure 3.1h**). Both static and flow cell biofilm models confirm D-CNPs were more effective at dispersing mature, amyloid rich *S. aureus* biofilms.

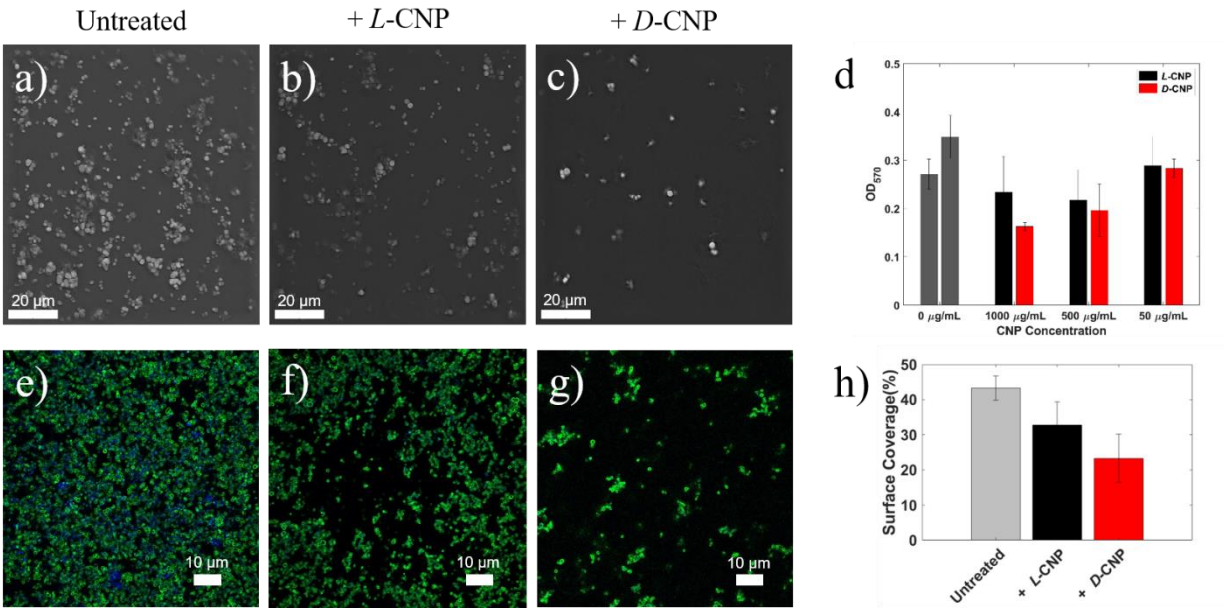

Figure 3.3 Scanning electron microscopy images of a) untreated biofilm and b) *L*-CNPs and c) *D*-CNPs treated biofilms grown statically for 24 hrs. d) Quantified CV staining of static biofilms. Confocal microscopy images of e) untreated and f) *L*-CNPs and g) *D*-CNPs treateded biofilms grown in dynamic flow cells for 3 days. Bacterial cells are stained with DAPI (blue) and polysaccharide intercellular adhesin (PIA) were stained with wheat germ agglutinin(green) h) calculated surface coverage of biofilms grown in flow cells.

D-CNPs displaying stronger interactions with *S. aureus* biofilms than *L*-CNPs is expected, as *D*-amino acids have been found to cause biofilm dispersal.[33–35] *D*-amino acids have been found in mature biofilms and have been hypothesized to signal biofilm dispersal due to lack of nutrients and an accumulation of metabolic waste.[34] The *D*-CNPs are potentially mimicking *D*-amino acids as signaling molecules and initiating premature biofilm dispersal. Furthermore, bacteria are known to incorporate *D*-amino acids for regulating peptidoglycan synthesis and maintenance, a key component of the bacterial cell wall. Enzymes responsible for peptidoglycan regulation could be trying to incorporate the *D*-cysteine molecules located at the CNP surface into the EPS network which anchors bacterial cells to surrounding exopolymers. Furthermore, the chirality of *D*-CNPs is the opposite handedness of the amyloid fibers located in the EPS. *D*-CNPs may experience weaker self-assembly and reversibly attach and dissociate in multiple locations within the EPS.

3.2.3 Chiral Carbon Nanoparticles and Planktonic S. aureus

It's important to note that chiral CNPs do not influence planktonic bacteria cell growth. We took both enantiomers of the CNPs and conducted a minimum inhibition concentration assay. Neither the *L*- nor *D*-CNPs, regardless of the dosage, were able to inhibit *S. aureus* cell growth (**Figure B2**). This indicates that the primary mechanism for biofilm dispersal is by interacting with the EPS matrix rather than *via* toxicity to the individual bacterial cells.

3.2.4 Chiral Chromatography of Biofilm Supernatant

To ensure the CNPs are stable and do not degrade back into their precursor cysteine or other small molecule derivatives, the supernatant after the biofilm treatment with chiral CNPs was analyzed by chiral HPLC. The elution times of *rac*-cysteine was taken as a control. Both cysteine enantiomers as well as other small molecules have retention times longer than 3 minutes with *D*-CNPs retaining longer on the chiral column (**Figure S3**). The supernatant of *L*- and *D*-CNP treated biofilms do not contain peaks beyond 3 minutes indicating the CNPs are intact. The retention time of chiral CNPs is identical to those observed before,[31] which indicates their hydrolytic and proteolytic stability in bacterial media as opposed to antimicrobial peptides or enzymes.

3.2.5 ThT Fibrillation Assay

Amyloid fibers with *S. aureus* are composed of short α-helical amphipathic peptides called phenol soluble modulins (PSMs). PSMs play a significant role in bacteria pathogenicity and virulence. PSMs are involved in many biological processes including biofilm formation, cytolysis, and immune system modulation.[36–38] PSMα1 and PSMα3 are two PSM peptides capable of assembly into amyloid-like fibers. Achiral graphene quantum dots have been reported to mimic peptide binding biomolecules to form supramolecular assemblies with PSMs and interfere with the self-

assembly into amyloid fibers.[27] We anticipate C^3NPs will bind enantioselectively PSMs and disturb assembly into mechanically flexible fibers necessary for biofilm stability.

The effect of chiral CNPs on commercially available, synthetic PSMα1 and PSMα3 aggregation kinetics was monitored experimentally using a Thioflavin T (ThT) assay. ThT is a stain that emits strong fluorescence when bound to β-sheets within amyloid fibers.[39] An increase in ThT intensity indicates PSMs are assembling into fibrillar species. Chiral CNPs were incubated with synthetic PSMα1 and PSMα3 for 24 hrs at 37°C (**Figure 3.4a**). For PSMα1 and PSMα3 alone, no aggregation was observed under these conditions. When chiral CNPs were co-incubated with PSMα1, ThT intensity increased indicating that both enantiomers facilitate fibrillation (**Figure 3.4b**). The rate of fibrillation for PSMα1 was similar when incubated with both chiral CNPs enantiomers indicating chirality did not affect the rate of PSMα1 self-assembly.

In case of PSMα3, a rise in ThT fluorescence can be observed when this amyloid forming peptide is incubated with chiral CNPs (**Figure 3.4c**) and there is a clear enantioselectivity. Unlike PSMα1,ThT fluorescence increased more rapidly for PSMα3 when incubated with *L*-CNPs compared to *D*-CNPs. The difference in the rate of PSMα3 ThT fluorescence and chiral CNPs suggest PSMα3 may have a higher affinity for *L*-CNPs or chiral CNPs are causing PSMα3 to assemble into unique structures based on the surface chirality of the NP. The PSMα1 and PSMα3 aggregation follows the secondary nucleation mechanism[40] that can be described as nucleus formation catalyzed by existing aggregates.[40,41] Chiral CNPs likely mimic preformed fibril seeds which allows PSM peptides to bypass the primary nucleation rate-limiting step and accelerates the aggregation process of PSMα1 and PSMα3.

To investigate further the chiral preferences, MD simulations were used to understand the aggregation of PSM peptides onto chiral CNPs. PSMs not only aggregate on the CNP, but this

aggregation seeds further clustering of PSMs. Up to four layers were observed, with outer layers sometimes composed of a single peptide, but this process could be even more prominent, as peptide deposition on layers and layer reorganization happen on a longer timescale than the one simulated here. While aggregation and seeding are observed for all the systems (**Figure 3.4d-g**), the PSMα3/*L*-CNP aggregate is the only system that forms two stable layers, while the other systems have four. This difference is more significant when considering that more PSMα3 peptides aggregate around *L*-CNP (all 15 peptides), compared to the nine of them that aggregate on *D*-CNP, suggesting that *L*-CNP could not only bind PSMα3 strongly, but could also favor a better spatial organization that leads to a more efficient clustering. This effect is not observed for the PSMα1/*L*-CNP aggregate, likely because the long-lived hydrogen bonds are localized more toward the end of the peptide, allowing higher configurational freedom that results in a more disorganized assembly as indirectly shown by more spread distribution of peptides (**Figure 3.4d**).

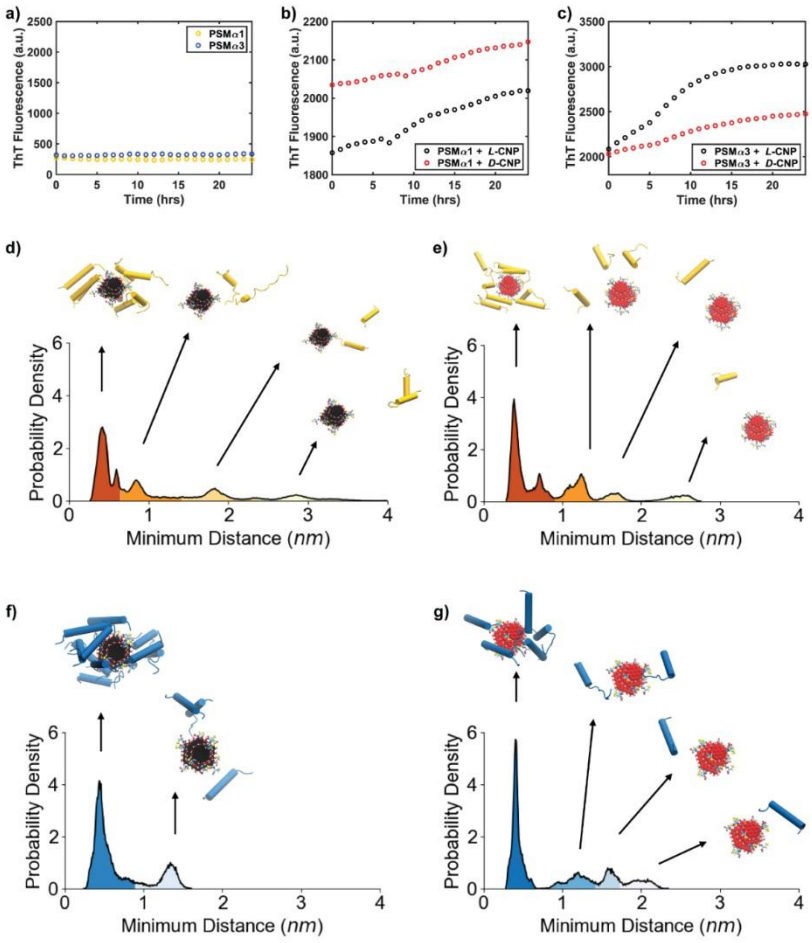

Figure 3.4: CNPs seed the formation of PSM aggregates. ThT fluorescence assay of a)PSM1 and PSM3 b) PSMα1 and cCNPs b) PSMα3 cCNPs. (d-e) PSMα1 (yellow palette) aggregating around (d) *L*-CNP (black) and (e) *D*-CNP (red). (f-g) PSMα3 (blue palette) aggregating around (f) *L*-CNP (black) and (g) *D*-CNP (red). The distributions are collected during the group simulations, where the minimum distance is taken between each amino acid on the PSM considering only non-hydrogen atoms on the surface of the CNP.

A more quantitative description of the differences between the orientations of the peptides aggregated on CNPs cannot be surmised from the MD simulations performed. Nevertheless, it is worth noting that the peptides aggregating with respect to the CNP surface in a variety of orientations (**Figure 3.5)** indicating the agglomeration in multiple conformations that is likely to lead to highly imperfect non-crystalline agglomerates.

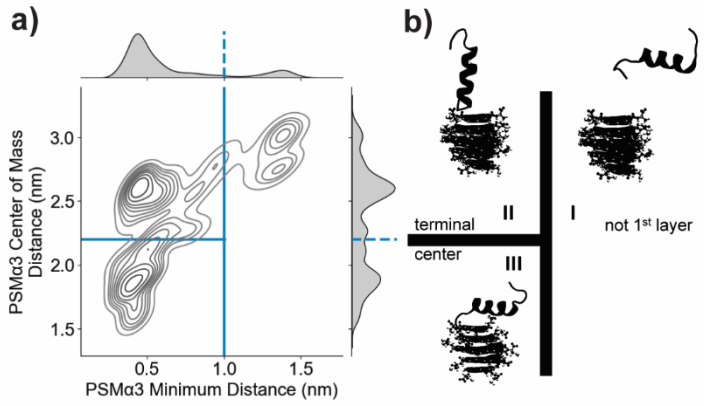

Figure 3.5: a) The distribution of configuration as a function of the minimum distance (between the *L*-CNP surface and all the PSMα3 atoms) and PSMα3 center of mass distance. Isolines of the smoothed data (using a Gaussian kernel function) are shown in gray. b) Projected distributions on single dimensions are shown on the right and top. Blue lines indicate approximate grouping of confirmation, as explained in the right panel.

3.2.6 CNPs affect PSM Secondary Structure

Changes in the secondary structure of the PSM peptides after incubation with chiral CNPs were monitored using circular dichroism (CD). After 24hrs, PSMα1 alone contains two negative bands at 210 nm and 220 nm which suggests PSMα1 is mostly composed of α-helices (**Figure 3.6a**).[42] After incubation with chiral CNPs, a single negative peak can be seen at 225 nm which suggests PSMα1 transitions from α-helices to β-pleated sheets. Similar trends can be seen when chiral CNPs are incubated with PSMα3. PSMα3 incubated alone displays double local minima near 210 nm and 220 nm indicative of α-helices. After 24 hr incubation with chiral CNPs, a single negative peak is observed at 230 nm which suggests the formation of β-pleated sheets (**Figure 3.6b**). CD spectra do not highlight any chiral discrimination interactions between CNPs and PSMs. However, in the case of both PSMα1 and PSMα3, chiral CNPs facilitate transitions from α-helices to β-pleated sheets which suggests amyloid fibril formation. MD simulations confirmed the chiral CNPs cause PSM peptides transitions from α-helices to β-sheets (**Figure 3.6c**). While all PSMs show some loss of α-helical secondary structure when interacting with CNP, compared to when

they are solvated in water, this change is almost negligible for PSMα3. For both PSMs, the slight loss of α-helix corresponds to a roughly equal increase in random coil and β-sheet, independently of the CNP chirality; however, we observe a much more relevant loss of the α-helical secondary structure with both CNPs for PSMα1. Moreover, for PSMα1, this change results primarily in an increase of β-sheet and some random coil secondary structure. This difference between the peptides, is likely due to the higher stability of the PSMα1 β-aggregates[43], and is likely responsible for the observed differences in the structure of the additional layers of peptides, as discussed above and shown in **Figure 3.5**.

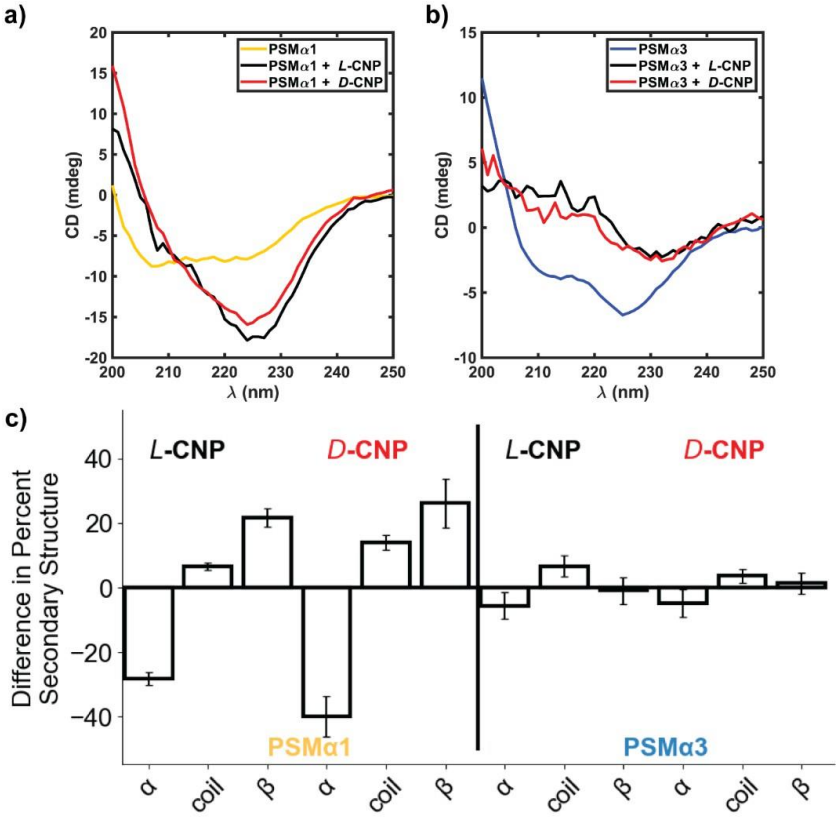

Figure 3.6: Change in structure of PSMs due to interactions with CNP. (a-b) Add caption for experimental images (c) Bars show the difference in secondary structure compared to the solvated peptides as sampled in the single PSM simulations. Error bars are standard errors of the mean. Negative values indicate a reduction in the secondary structure interacting with CNPs.

3.2.7 Morphology of PSM-CNP Supramolecular Assemblies

The morphology of PSM/CNP assemblies were investigated using transmission electron microscopy (TEM) after 24 hr co–incubation. At *t* = 0 in **Figure A**, PSMα1 displayed small, prefibrillar oligomers which confirms the absence of ThT fluorescence increase in **Figure 3.3**. PSMα1 assembled into spherical oligomers in the presence of *L*-CNPs while *D*-CNPs caused PSMα1 to remain as pre-fibrillar aggregates (**Figure A.4a and A.4b**). After 24 hr incubation with both C^3NPs enantiomers, PSMα1 began to assemble into wide diameter nanotubes (apparent width ~100 nm to 400 nm) (**Figure 3.7b and 3.7c**). This indicates that C^3NPs alter but do not inhibit fibrillation pattern of PSMα1. The nanotubes appear to have the same size and shape when PSMα1 is incubated with either CNP indicating minimal stereospecific effects on the morphology of the PSMα1/CNP assemblies. Chiral CNPs mediated assembly of PSMs in nanotubes regardless of the handedness of the particle also explains why the increase in the rates of ThT intensity was similar in **Figure 3.4**. PSM nanotube assemblies have been previously described for PSMα3 but not for PSMα1.[44–46] To the best of our knowledge, this is the first report of PSMα1 achieving nanotube confirmations, and CNP catalyzed peptide assembly into nanotubes has also not been previously described. The formation of rigid nanotubes differs strongly from the native structure within the EPS matrix and likely inhibits cooperativity with other EPS components and reduces biofilm stability.

Supramolecular assemblies formed between C^3NPs and PSMα3 can be seen using TEM. At *t* = 0, PSMα3 incubated alone and with *D*-CNPs remains as amorphous aggregates. However, *L*-CNPs cause PSMα3 to immediately assemble into fibril networks (**Figure A.4a-A.4c**). Chiral discrimination of PSMα3 interactions with chiral CNPs can be seen after 24 hrs as well. After 24 hr incubation, it's apparent that PSMα3 alone does not fibrillate at these conditions (**Figure 3.7d**). After 24 hrs, we see that *L*-CNP/PSMα3 fibrils seen at t = 0 begin to wrap around each other to

form twisted filament structures while *D*-CNP treated PSMα3 transitioned from amorphous aggregates to more defined spherical oligomers (**Figure 3.7e and 3.7f**). PSMα3 is known to nucleate and catalyze assembly of PSMα1 into biofilm stabilizing nanofibrils.[40] C^3NPs prevent nucleation and distort helical conformations of PSMs within the EPS. The handedness of the CNPs causes PSMα3 to assemble into unique structures which may be an explanation for the observed differences in rate of ThT fluorescence increase (**Figure 4**).

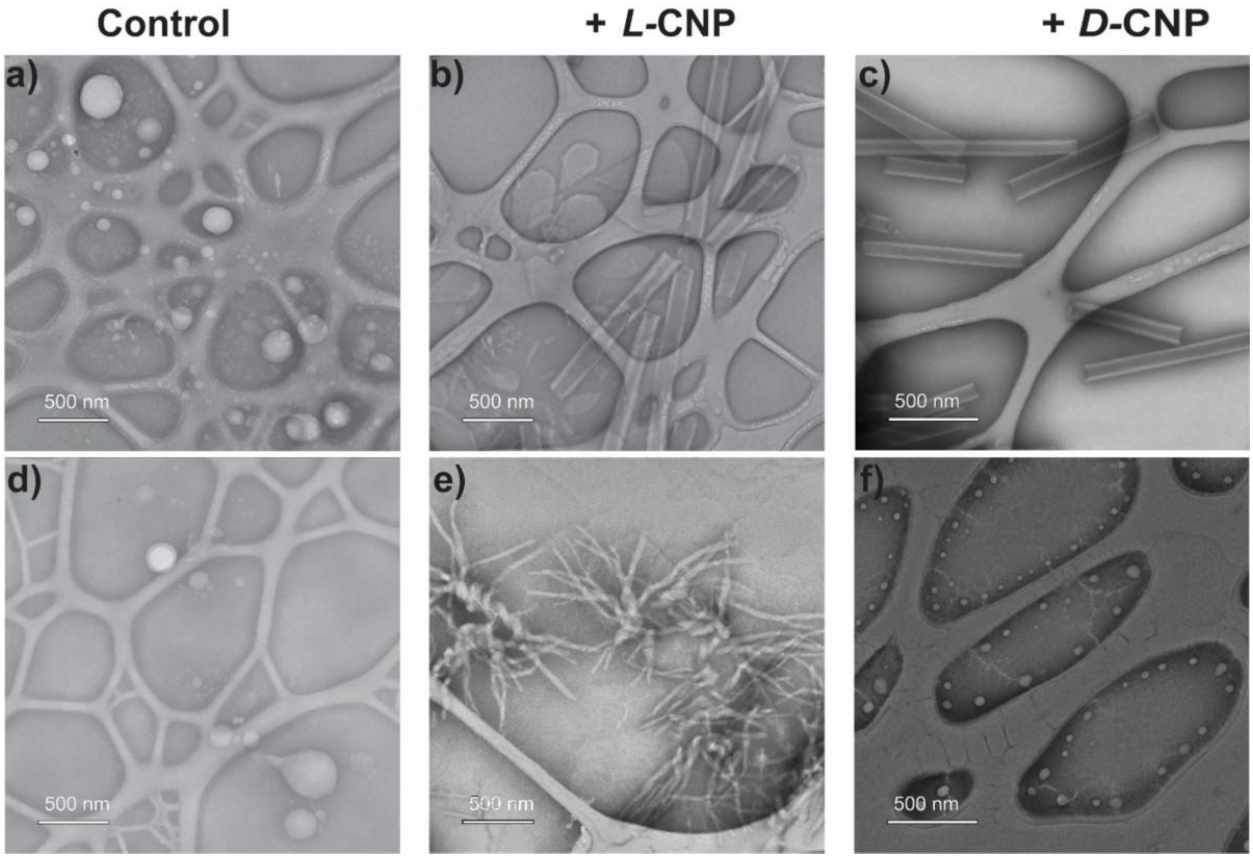

Figure 3.7: TEM images at t = 24 hrs for a) PSMα1 b) PSMα1 + *L*-CNPs c) PSMα1 + *D*-CNPs d) PSMα3 e) PSMα3 + *L*-CNPs f) b) PSMα3 + *D*-CNPs.

3.2.8 PSMs bind to CNPs with chiral specificity

In all simulations, we observe that the peptides will form long-lasting interactions with the CNPs. Specifically, we detect the formation of long-lived hydrogen bonds between the PSMs and the nanoparticles, with an average of about 8 peptides directly interacting with the CNP. While the

interactions involve a variety of residues, from N-terminus to C-terminus and other more central residues, lysine (LYS) residues show significant specificity in their preference for *L*-CNP over *D*-CNP. As shown in **Figure 3.8**, LYS residues on both PSMs form longer living hydrogen bonds with *L*-CNP.

This chiral specificity is not limited to LYS groups, but it also extends to Asparagine (ASN), namely ASN21 and ASN22 (present only on PSMα3), which form bonds with *D*-CNP with an average lifetime of 13.4 ± 4.3 ps and 3.7 ± 0.6 ps, respectively(**B.5**). These lifetimes are remarkably longer than the ones observed for PSMα3/*L*-CNP (0.12 ± 0.01 ps and 0.09 ± 0.01 ps), suggesting that, for PSMα3, the short-lived interactions of the LYS groups are compensated with longer-lived ASN h-bonds.

Both LYS and ASN residues play an important role in the structure and functionality of PSM peptides. PSMs' LYS residues have been shown to be essential for protein stability and interactions with other molecules.[47] Post-translational modification of LYS residues significantly enhances protein aggregation, including into amyloid fibers, through a mechanism that involves the PTM shielding the positive charge of the LYS residue, decreasing electrostatic repulsive forces, and promoting aggregation.[48] Lysine residues are also responsible for the inter-protofilament salt-bridge interactions of PSM amyloid fibers[43]. ASN21 and ASN22 have been shown to be important in the recognition of PSMα3 during the formyl peptide receptor 2 (FPR-2)-mediated pro-inflammatory response.

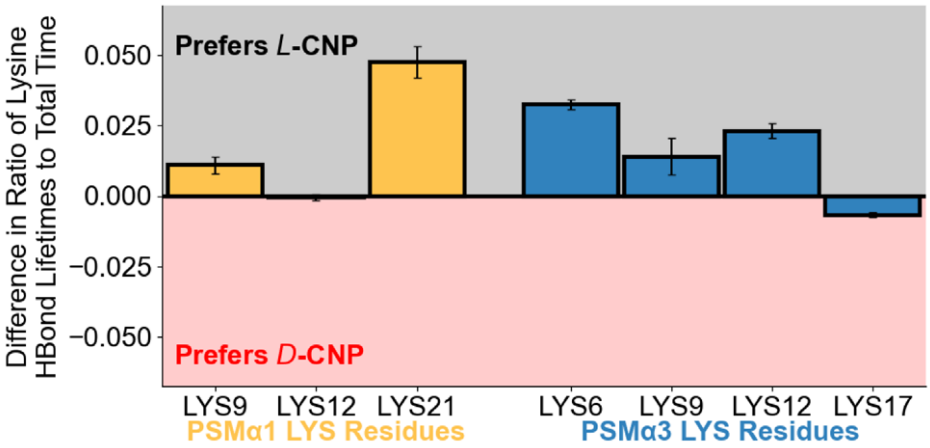

Figure 3.8: Molecular dynamics simulations collected a) hydrogen bond lifetimes between cCNPs and LYS residues of PSMs. Data is collected from group simulations. Error bars are standard errors of the mean, taken at 5ns intervals of the trajectory. All hydrogen bond lifetimes are positive and have been normalized by the 5ns of total simulation time.

3.2.9 Modulation of PSM Hemolytic Activity

PSM peptides, notably PSMα3, are known to be cytotoxic towards mammalian cells. [29,49,50] To assess the effect of chiral CNPs on the cytolytic properties of PSM peptides, PSMα1 and PSMα3 were incubated with red blood cells (RBCs) and chiral CNPs and hemolysis was quantified by hemoglobin absorption in the supernatant **(Figure 3.9)**. When PSMα1 was incubated with RBCs, cell viability was reduced by about 40% (**Figure 3.9a**). *L*-CNPs were able to reduce the lysing capabilities of PSMα1 by about 10%. In the presence of *D*-CNPs, PSMα1 exacerbated RBC lysis eliciting higher hemolytic activity than being incubated alone with RBCs alone or when treated with *L*-CNPs **(Figure 3.9a)**. PSMα3 is notorious for being the most cytotoxic PSM peptide and showed greater lytic activity than PSMα1 (**Figure 3.9a & 3.9b**).[45] Both CNP enantiomers were able reduce the hemolytic activity of PSMα3. Similar to PSMα1, there were more viable RBCs when PSMα3 was incubated with *L*-CNPs rather than *D*-CNPs. It should be noted that cytotoxicity of both CNP enantiomers is negligible but *D*-CNPs did have slightly more adverse effect to RBCs than *L*-CNPs (**Figure 3.9c**).

The proposed mechanism for PSM mediated lysis is by disruption of cell membranes in a receptor-independent manor similar to antimicrobial peptides.[37,38,49] It's likely that the PSM/CNP supramolecular structures are causing lysis through membrane-disrupting mechanisms as well. The spherical shape of PSMα1/*L*-CNP assemblies is less toxic than the amorphous aggregates produced by PSMα1/*D*-CNP. The structure of PSMα1/D-CNP more resembles PSMα1, but the hemolytic effect was less pronounced. This highlights that the CNPs likely decorate the surface of these assemblies and difference is surface chirality causes stereoselective hemolysis. Amino acids and peptides preferentially interact with lipids of the same chirality.[52,53] So, it can be hypothesized that PSMα1/*D*-CNP supramolecular structure's spatial orientation and surface chirality interacts less favorably with the *L*- configuration of phospholipids within red blood cells (RBCs) membranes resulting in increased disruption of the lipid bilayer and ultimately lysis. Similar analysis can be said for PSMα3. The results from the hemolysis assay suggest *L*-CNPs are more favorable than *D*-CNPs when trying to reduce the hemolytic properties of PSM peptides.

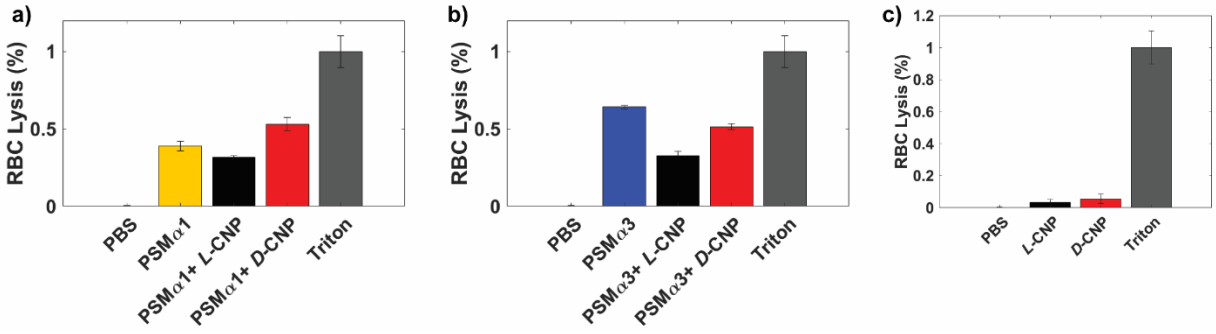

Figure 3.9: Hemolytic activity of a) PSMα1/CNP and b) PSMα3/CNP assemblies c) cCNPs

3.2.10 Chiral CNPs Effect on PSMα3 Mediated IL-8 Production

All PSMs are known to be pro-inflammatory mediators including the activation of neutrophils triggering the release of cytokines, such as interleukin-8 (IL-8).[30,54] The effect of chiral CNPs on PSMα3 mediated IL-8 production was assessed using an enzyme linked immunosorbent assay

(ELISA) in **Figure 3.10**. *L*-CNPs slightly enhanced PSMα3 production of IL-8 while *D*-CNPs were able to inhibit cytokine release. IL-8 release is mediated by N-formyl peptide receptor 2 (FPR2) recognition of PSMs, with the lysine side chains responsible for initiating a inflammatory response .[30,38] It is likely that both CNP enantiomers are electrostatically interacting with the cationic side chains of PSMα3 but the PSMα3/*L*-CNP complex is likely recognized by the *L*-configuration of the FPR2 receptor, resulting in release of IL-8. On the contrary, the PSMα3/ *D*-CNP complex does not have the correct spatial orientation to bind favorably to FPR2 receptor, resulting in a reduction of IL-8 production.

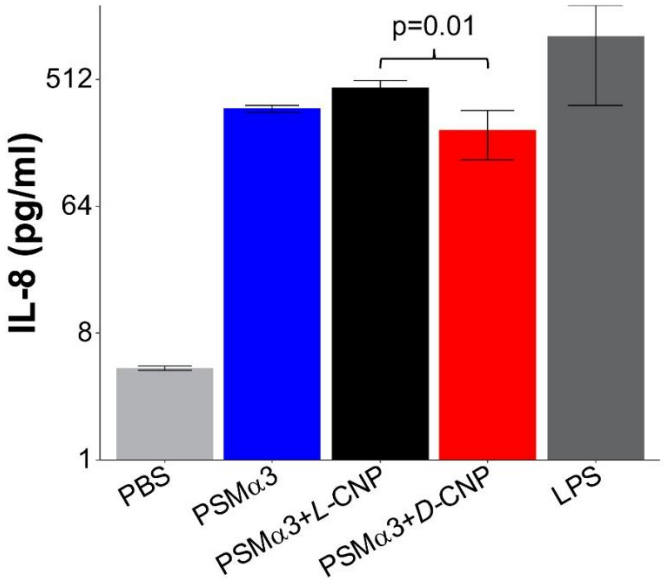

Figure 3.10: Effect of Chiral CNPs on PSM-mediated Il-8 production.

3.3 Conclusions

In this work, we showed cysteine-derived chiral CNPs can disperse amyloid-rich *S. aureus* biofilms with *D*-CNPs displaying higher anti-biofilm activity than *L*-CNPs. Integrating the data from chiroptical spectroscopy and MD simulation, we show that interactions of CNPs with peptides forming amyloid nanofibers are essential for understanding the mechanism of the biofilm dispersal. *D*-CNPs act favorably when dispersing biofilms, but *D*-CNPs enhance the virulence

properties of PSMs compared to *L*-CNPs. This merits additional studies to understand the dosage necessary to disseminate biofilms while mitigating the virulence properties of free floating PSM peptides. Additional modifications of CNPs to achieve the desired effects include changing the physicochemical properties of the nanoparticles. The results of this work prove that CNPs are a promising anti-biofilm platform.

3.4 Experimental

3.4.1 Materials.

L-cysteine, *D*-cysteine, and sodium hydroxide (NaOH) were purchased from Millipore Sigma. *DL*-cysteine was prepared by mixing equal amounts of pure *L*-cysteine and *D*-cysteine at 1 mg m*L*-^{1}. Dialysis tubes with molecular weight cut off of 1kDa were obtained from Fischer Scientific. Acetonitrile (HPLC grade) was purchased from Millipore Sigma. All solutions were prepared using ultrapure water (18.2 MΩ·cm).

3.4.2 Static Biofilms.

S. aureus USA300 from -80°C glycerol stock was plated on tryptic soy agar. Single colony inoculates were grown overnight to mid log. Overnight cultures were centrifuged and washed with PBS then suspended in PNG media. This suspension was then seeded in µ-slide I luer chambers and grown for 24 hrs at 37°C. After 24hrs, the chambers were washed with 1X PBS to remove unadhered cells and debris. The biofilms were then fixed with 2% paraformaldehyde for 15 minutes then washed with 1X PBS. The biofilms were suspended in ultrapure waster for nanolive imaging.

3.4.3 Flow Cell Biofilms.

S. aureus USA300 from -80°C glycerol stock was plated on tryptic soy agar. Single colony inoculates were grown overnight to mid log. Overnight cultures were centrifuged and washed with PBS, then resuspended in PNG media. This suspension was seeded in single chamber flow cells for 1 hr. Biofilms were then allowed to grow for 72 hrs in PNG media under flow at 13 µl min^{-1}. Then, 0 or 500 µg mL^{-1} of *L*- or *D*-CNPs was added before flow resumed for an additional 24 hrs.

3.4.4 *Synthesis of L- or D-CNPs.*

Chiral CNPs were synthesized by a hydrothermal method as previously described.[55] 0.5 g of *L*-cysteine (*L*-cys) or *D*-Cysteine (*D*-cys) and 1g NaOH was dissolved in 10 mL of water under ultrasonification for 20 minutes. The prepared solution was transferred into a 25 mL Teflon lined autoclave and heated at 120 °C for 16h. The mixture was dialyzed to remove unreacted material for 3 days. The final product was filtered against a 0.22-micron filter to remove large aggregates and then lyophilized for storage.

3.4.5 *Chiral HPLC Analysis.*

Chiral CNPs were separated Agilent 6000 Series LC/MS instrument HPLC using an Astec CHIROBIOTIC T 10 cm x 4.6 mm (Millipore Sigma) chiral column. The mobile phase consisted of ultrapure water and acetonitrile (30:70 v/v) applied over 10 minutes at a flow rate of 1 mL min^{-1}. UV detection was set to 205 nm.

3.4.6 *Peptide Preparation*

PSMα1 and PSMα3 were purchased from XX with >90% purity. They were dissolved to a final concentration of 0.5 mg mL^{-1} in a 1:1 mixture of trifluoroacetic acid (TFA) and hexafluoroisoproponal (HFIP). The peptide solutions were sonicated for 20 minutes then incubated for 1 hr at room temperature. The stock solution was divided into aliquots and TFA/HFIP solvent

was evaporated using a speedvac and finally stored at -80°C. Peptides were suspended in 10% dimethlysulfoxide (DMSO) and sonicated for 20 minutes prior to use.

3.4.7 Thioflavin T Assay

Reconstituted peptides were diluted to 0.5 mg/mL in a solution containing 40 µM ThT solution (prepared in ultrapure water) and 2 mg/mL CNPs in a final volume of 200 µL in a 96-well black polystyrene microtiter plate. ThT fluorescence was measured at 37 °C under quiescent conditions. ThT fluorescence was monitored every hour for 24 hrs using an excitation filter of 450 nm and an emission filter of 482 nm.

3.4.8 Transmission Electron Microscopy

Carbon coated 400 mesh grids were faced with the copper facing down. 500 ug/mL of PSMs were treated with 2 mg/mL of CNPs and monitored over a 24 hr period. 10 ul of the PSM/CNP solution were placed on the carbon coated side of the TEM grid for 60 s. The grids were blotted dry and, then, treated with a 1% (w/v) of phosphotungstic acid for 60s. Grids were blotted dry and stored under vacuum prior to imaging.

3.4.9 Circular Dichroism

3.4.10 Hemolysis Assay

Red blood cells (RBCs) were diluted to 4% in Hank's balanced salt solution (HBSS). Then, 50 uL of RBC solution were transferred to a 96-well plate. CNPs and PSMs were added to each well and incubated at 37 °C for 1 hr. Spin the plate down at 300 g for 10 minutes to pellet intact RBCs. Then, the supernatant was removed and transfered to a new 96 well plate. Read at 405 nm on a plate-reader.

3.4.11 ELISA Assay

Neutrophils were isolated from whole blood using the EasySep Neutrophil Isolation Kit (cat #19666). Isolated cells were treated with CNPs and PSMs. IL-8 production after CNP/PSM treatment was monitored using the Quantikine Human IL-8/CXCL8 kit (D8000C). The assays were performed following the manufacturer's instructions.

3.4.12 Molecular Dynamics Simulations

All atom interactions were computed using CHARMM, version 36[56] and TIP3P water[57] force fields. NAnoscale Molecular Dynamics software[58] was used for running the simulations. First, systems were minimized and, then, equilibrated in the isothermal-isobaric ensemble until the root-mean-square deviation of the aggregate converged (between 60 and 200 ns). A global system pressure of 100 kPa was maintained using a Langevin piston Nose-Hoover method (with a period of 200 fs and 50 fs decay)[59,60] , and a Langevin thermostat[61] (with a characteristic time of 5 ps) was used to keep the system temperature at 300 K. A time step of 2 fs was employed to integrate the equations of motion, and all hydrogen bonds were kept rigid via the SHAKE algorithm[62]. Non-bonded short-range interactions smoothly approached 0 using an X-PLOR switching function[63] between 1 nm and the cutoff (1.2 nm), while long-range Coulombic forces were included using the particle mesh Ewald method[64] (with a tolerance of 1e-5).

We performed two sets of simulations (**Figure S5**), one aimed at understanding the specific interactions between peptide and nanoparticle (a single PSM + 1 CNP) and one to emulate a strong local concentration of PSMs (a group of 15 PSMs + 1 CNP).

To create a reasonable initial configuration of a single PSM interacting with a CNP, we used HDOCK[65], by taking the top 10 most likely binding configurations of each PSM with each layer of each CNP. Of the resulting 120 configurations (2 PSMs x 2 CNPs x 3 molecules in each CNP

x 10 predictions), only about 14% (17 configurations) were not discarded due to nonphysical atomic overlap. All these configurations were equilibrated using the protocol described above, but systems that did not equilibrate within 200 ns were discarded, leaving only 11 systems (3 for PSMα1/*D*-CNP, PSMα3/*D*-CNP, and PSMα3/*L*-CNP, and 2 for PSMα3/*L*-CNP).

The systems with 15 PSMs were generated by randomly placing the peptides around the CNP at an center of mass distance between 3 and 4 nm. PLUMED[66] was used to place a harmonic limit on the distance between the centers of mass of each PSM and the CNP at 6 nm with a force constant of 100 kcal/mol. Visual Molecular Dynamics[67] was used for molecular visualization and secondary structure analysis. MDAnalysis[68] and Matplotlib[69] Python libraries were used for data processing and visualization. Hydrogen bond lifetimes were calculated using MDAnalysis, where (1) tau_max was set to 5 ns, (2) intermittency was set to 1, and default values of 0.3 nm and 150^{o} were used for the (3) d_h_cutoff (hydrogen bond distance) and (4) d_h_a_cutoff (hydrogen bond angle), respectively.

3.5 References

1. Costerton, J. W., Stewart, P. S. & Greenberg, E. P. Bacterial biofilms: a common cause of persistent infections. *Science* **284**, 1318–22 (1999).
2. Beckwith, J. K., VanEpps, J. S. & Solomon, M. J. Differential Effects of Heated Perfusate on Morphology, Viability, and Dissemination of Staphylococcus epidermidis Biofilms. *Appl Environ Microbiol* **86**, (2020).
3. Fulaz, S. *et al.* Tailoring nanoparticle-biofilm interactions to increase the efficacy of antimicrobial agents against Staphylococcus aureus. *Int J Nanomedicine* 4779–4791 (2020).

4. Hall-Stoodley, L., Costerton, J. W. & Stoodley, P. Bacterial biofilms: from the Natural environment to infectious diseases. *Nat Rev Microbiol* **2**, 95–108 (2004).

5. Stewart, P. S. Mechanisms of antibiotic resistance in bacterial biofilms. *International Journal of Medical Microbiology* **292**, 107–113 (2002).

6. Koo, H., Allan, R. N., Howlin, R. P., Stoodley, P. & Hall-Stoodley, L. Targeting microbial biofilms: Current and prospective therapeutic strategies. *Nature Reviews Microbiology* vol. 15 740–755 Preprint at https://doi.org/10.1038/nrmicro.2017.99 (2017).

7. Bhando, T., Dubey, V. & Pathania, R. Biofilms in Antimicrobial Activity and Drug Resistance. *Bacterial Adaptation to Co-resistance* 109–139 (2019).

8. Gebreyohannes, G., Nyerere, A., Bii, C. & Sbhatu, D. B. Challenges of intervention, treatment, and antibiotic resistance of biofilm-forming microorganisms. *Heliyon* **5**, (2019).

9. Hancock, R. E. W. & Sahl, H. G. Antimicrobial and host-defense peptides as new anti-infective therapeutic strategies. *Nature Biotechnology* vol. 24 1551–1557 Preprint at https://doi.org/10.1038/nbt1267 (2006).

10. Chung, P. Y. & Khanum, R. Antimicrobial peptides as potential anti-biofilm agents against multidrug-resistant bacteria. *Journal of microbiology, immunology and infection* **50**, 405–410 (2017).

11. Meng, H. & Kumar, K. Antimicrobial activity and protease stability of peptides containing fluorinated amino acids. *J Am Chem Soc* **129**, 15615–15622 (2007).

12. Azeredo, J., García, P. & Drulis-Kawa, Z. Targeting biofilms using phages and their enzymes. *Curr Opin Biotechnol* **68**, 251–261 (2021).

13. Malik, E., Dennison, S. R., Harris, F. & Phoenix, D. A. pH dependent antimicrobial peptides and proteins, their mechanisms of action and potential as therapeutic agents. *Pharmaceuticals* **9**, 67 (2016).

14. Hoan, B. T., Tam, P. D. & Pham, V. H. Green Synthesis of Highly Luminescent Carbon Quantum Dots from Lemon Juice. *J Nanotechnol* **2019**, (2019).

15. Chung, S., Revia, R. A. & Zhang, M. Graphene Quantum Dots and Their Applications in Bioimaging, Biosensing, and Therapy. *Advanced Materials* **33**, 1904362 (2021).

16. Elvati, P., Baumeister, E. & Violi, A. Graphene quantum dots: effect of size, composition and curvature on their assembly. *RSC Adv* **7**, 17704–17710 (2017).

17. Russ, K. A. *et al.* C 60 fullerene localization and membrane interactions in RAW 264.7 immortalized mouse macrophages. *Nanoscale* **8**, 4134–4144 (2016).

18. Zeng, Z., Chen, S., Tan, T. T. Y. & Xiao, F. X. Graphene quantum dots (GQDs) and its derivatives for multifarious photocatalysis and photoelectrocatalysis. *Catal Today* **315**, 171–183 (2018).

19. Garg, B. & Bisht, T. Carbon nanodots as peroxidase nanozymes for biosensing. *Molecules* **21**, 1653 (2016).

20. Kang, S. *et al.* Graphene Oxide Quantum Dots Derived from Coal for Bioimaging: Facile and Green Approach. *Sci Rep* **9**, (2019).

21. Sheng, L. *et al.* A highly selective and sensitive fluorescent probe for detecting Cr(VI) and cell imaging based on nitrogen-doped graphene quantum dots. *J Alloys Compd* **820**, 153191 (2020).

22. Iannazzo, D. *et al.* Graphene quantum dots for cancer targeted drug delivery. *Int J Pharm* **518**, 185–192 (2017).

23. Zhao, D. *et al.* The preparation of chiral carbon dots and the study on their antibacterial abilities. *Mater Chem Phys* **295**, 127144 (2023).

24. Victoria, F., Manioudakis, J., Zaroubi, L., Findlay, B. & Naccache, R. Tuning residual chirality in carbon dots with anti-microbial properties. *RSC Adv* **10**, 32202–32210 (2020).

25. Malishev, R. *et al.* Chiral modulation of amyloid beta fibrillation and cytotoxicity by enantiomeric carbon dots. *Chemical Communications* **54**, 7762–7765 (2018).

26. Arad, E. *et al.* Lysine-derived carbon dots for chiral inhibition of prion peptide fibril assembly. *Adv Ther (Weinh)* **1**, 1800006 (2018).

27. Wang, Y. *et al.* Anti-Biofilm Activity of Graphene Quantum Dots via Self-Assembly with Bacterial Amyloid Proteins. *ACS Nano* **13**, 4278–4289 (2019).

28. Šiširak, M., Zvizdić, A. & Hukić, M. Methicillin-resistant Staphylococcus aureus (MRSA) as a cause of nosocomial wound infections. *Bosn J Basic Med Sci* **10**, 32 (2010).

29. Cheung, G. Y. C., Joo, H.-S., Chatterjee, S. S. & Otto, M. Phenol-soluble modulins – critical determinants of staphylococcal virulence. *FEMS Microbiol Rev* **38**, 698–719 (2014).

30. Peschel, A. & Otto, M. Phenol-soluble modulins and staphylococcal infection. *Nat Rev Microbiol* **11**, 667–673 (2013).

31. Hubbard, M. A. *et al.* Chiral chromatography and surface chirality of carbon nanoparticles. *Chirality* **34**, 1494–1502 (2022).

32. Kamiński, M., Kudelski, A. & Pecul, M. Vibrational optical activity of cysteine in aqueous solution: A comparison of theoretical and experimental spectra. *Journal of Physical Chemistry B* **116**, 4976–4990 (2012).

33. Hochbaum, A. I. *et al.* Inhibitory Effects of D-Amino Acids on Staphylococcus aureus Biofilm Development †. *J Bacteriol* **193**, 5616–5622 (2011).

34. Kolodkin-Gal, I. *et al.* D-Amino acids trigger biofilm disassembly. *Science (1979)* **328**, 627–629 (2010).

35. De La Fuente-Núñez, C. *et al.* D-Enantiomeric Peptides that Eradicate Wild-Type and Multidrug-Resistant Biofilms and Protect against Lethal Pseudomonas aeruginosa Infections. *Chem Biol* **22**, 196–205 (2015).

36. Schwartz, K., Syed, A. K., Stephenson, R. E., Rickard, A. H. & Boles, B. R. Functional amyloids composed of phenol soluble modulins stabilize Staphylococcus aureus biofilms. *PLoS Pathog* **8**, (2012).

37. Da, F. *et al.* Phenol-soluble modulin toxins of Staphylococcus haemolyticus. *Front Cell Infect Microbiol* **7**, 206 (2017).

38. Cheung, G. Y. C. *et al.* Insight into structure-function relationship in phenol-soluble modulins using an alanine screen of the phenol-soluble modulin (PSM) α3 peptide. *The FASEB Journal* **28**, 153–161 (2014).

39. Xue, C., Lin, T. Y., Chang, D. & Guo, Z. Thioflavin T as an amyloid dye: Fibril quantification, optimal concentration and effect on aggregation. *R Soc Open Sci* **4**, (2017).

40. Zaman, M. & Andreasen, M. Cross-talk between individual phenol- soluble modulins in staphylococcus aureus biofilm enables rapid and efficient amyloid formation. *Elife* **9**, 1–17 (2020).

41. Najarzadeh, Z. *et al.* Heparin promotes fibrillation of most phenol-soluble modulin virulence peptides from Staphylococcus aureus. *Journal of Biological Chemistry* **297**, (2021).

42. Greenfield, N. J. Using circular dichroism spectra to estimate protein secondary structure. *Nat Protoc* **1**, 2876–2890 (2006).

43. Elvati, P. *et al.* Molecular Architecture and Helicity of Bacterial Amyloid Nanofibers: Implications for the Design of Nanoscale Antibiotics. *ACS Appl Nano Mater* (2021).

44. Kreutzberger, M. A. B. *et al.* Phenol-soluble modulins PSMα3 and PSMβ2 form nanotubes that are cross-α amyloids. *Proceedings of the National Academy of Sciences* **119**, (2022).

45. Tayeb-Fligelman, E. *et al.* The cytotoxic Staphylococcus aureus PSMα3 reveals a cross-α amyloid-like fibril. *Science (1979)* **355**, 831–833 (2017).

46. Malishev, R. *et al.* Reciprocal Interactions between Membrane Bilayers and S. aureus PSMα3 Cross-α Amyloid Fibrils Account for Species-Specific Cytotoxicity Correspondence to. (2018) doi:10.1016/j.jmb.2018.03.022.

47. Azami-Movahed, M., Meratan, A. A., Ghasemi, A., Ebrahim-Habibi, A. & Nemat-Gorgani, M. Acetylation of lysine residues in apomyoglobin: Structural changes, amyloid fibrillation, and role of surface charge. *Int J Biol Macromol* **107**, 626–634 (2018).

48. Azevedo, C. & Saiardi, A. Why always lysine? The ongoing tale of one of the most modified amino acids. *Adv Biol Regul* **60**, 144–150 (2016).

49. Laabei, M., Jamieson, W. D., Yang, Y., Van Den Elsen, J. & Jenkins, A. T. A. Investigating the lytic activity and structural properties of Staphylococcus aureus phenol

soluble modulin (PSM) peptide toxins. *Biochimica et Biophysica Acta (BBA) - Biomembranes* **1838**, 3153–3161 (2014).

50. Yao, Z. *et al.* Use of a Stereochemical Strategy to Probe the Mechanism of Phenol-Soluble Modulin α3 Toxicity. *J Am Chem Soc* **141**, 7660–7664 (2019).

51. Xuan, Q. *et al.* Salt-Inducing Assembly Polymorphism Strategy for Cytotoxicity Differentiation of Phenol-Soluble Modulin α3 Assemblies. *Biomacromolecules* **23**, 3318–3328 (2022).

52. Martin, H. S., Podolsky, K. A. & Devaraj, N. K. Probing the Role of Chirality in Phospholipid Membranes. *ChemBioChem* **22**, 3148–3157 (2021).

53. Sato, K., Ji, W., Lvarez, Z. A.́, Palmer, L. C. & Stupp, S. I. Chiral Recognition of Lipid Bilayer Membranes by Supramolecular Assemblies of Peptide Amphiphiles. *ACS Biomater Sci Eng* **5**, 2786–2792 (2019).

54. Bloes, D. A. *et al.* Phenol-soluble modulin peptides contribute to influenza A virusassociated Staphylococcus aureus pneumonia. *Infect Immun* **85**, (2017).

55. Hu, L. *et al.* Nitrogen and sulfur co-doped chiral carbon quantum dots with independent photoluminescence and chirality. *Inorg Chem Front* **4**, 946–953 (2017).

56. Huang, J. & Mackerell, A. D. CHARMM36 all-atom additive protein force field: Validation based on comparison to NMR data. *J Comput Chem* **34**, 2135–2145 (2013).

57. Jorgensen, W. L., Chandrasekhar, J., Madura, J. D., Impey, R. W. & Klein, M. L. Comparison of simple potential functions for simulating liquid water. *J Chem Phys* **79**, 926 (1998).

58. Phillips, J. C. *et al.* Scalable molecular dynamics with NAMD. *J Comput Chem* **26**, 1781–1802 (2005).

59. Feller, S. E., Zhang, Y., Pastor, R. W. & Brooks, B. R. Constant pressure molecular dynamics simulation: The Langevin piston method. *J Chem Phys* **103**, 4613–4621 (1995).

60. Martyna, G. J., Tobias, D. J. & Klein, M. L. Constant pressure molecular dynamics algorithms. *J Chem Phys* **101**, 4177–4189 (1994).

61. Loncharich, R. J., Brooks, B. R. & Pastor, R. W. Langevin dynamics of peptides: The frictional dependence of isomerization rates of N-acetylalanyl-N′-methylamide. *Biopolymers* **32**, 523–535 (1992).

62. Ryckaert, J. P., Ciccotti, G. & Berendsen, H. J. C. Numerical integration of the cartesian equations of motion of a system with constraints: molecular dynamics of n-alkanes. *J Comput Phys* **23**, 327–341 (1977).

63. Brünger, A. T. *X-PLOR: version 3.1: a system for x-ray crystallography and NMR*. (Yale University Press, 1992).

64. Darden, T., York, D. & Pedersen, L. Particle mesh Ewald: An N·log(N) method for Ewald sums in large systems. *J Chem Phys* **98**, 10089–10092 (1993).

65. Yang, B., Fu, X., Sidiropoulos, N. D. & Hong, M. Towards k-means-friendly spaces: Simultaneous deep learning and clustering. in *international conference on machine learning* 3861–3870 (PMLR, 2017).

66. Bonomi, M. *et al.* PLUMED: A portable plugin for free-energy calculations with molecular dynamics ☆. *Comput Phys Commun* **180**, 1961–1972 (2009).

67. Humphrey, W., Dalke, A. & Schulten, K. VMD: Visual molecular dynamics. *J Mol Graph* **14**, 33–38 (1996).

68. Michaud-Agrawal, N., Denning, E. J., Woolf, T. B. & Beckstein, O. MDAnalysis: a toolkit for the analysis of molecular dynamics simulations. *J Comput Chem* **32**, 2319–2327 (2011).

69. Hunter, J. D. Matplotlib: A 2D Graphics Environment. *Comput Sci Eng* **9**, 90–95 (2007).

Chapter 4 Conclusions and Future Directions

4.1 Summary and Key Takeaways

The studies presented in this dissertation highlight the synthesis and characterization of chiral CNPs for enantioselective dispersal of mature biofilms. In **Chapter 2**, chiral CNPs were synthesized using hydrothermal carbonization of *L*- and *D*- cysteine. Cysteine served as the source of carbon and the source of chirality. The origin of chirality within chiral CNPs was previously unknown, however using CD,VCD, and developing novel methods for HPLC separation of these nanoparticles confirmed there must be chiral centers located at the surface of the CNPs. The first report of chiral HPLC separation of chiral nanoparticles was achieved using a CHIROBIOTIC T chiral column with a simple water/acetonitrile mobile phase.[1] *D*-CNPs retained longer along the column while *L*-CNPs eluted about 10 seconds prior. The dominating forces behind the separation are steric hindrance and polar ionic. The CNPs were captured after separation and their physicochemical properties remained the same. This highlights the hydrolytic stability and recyclability of these nanoparticles. MD simulations were employed to understand the interactions between the chiral CNPs and teicoplanin, the macrocyclic glycopeptide based stationationary phase within the CHIROBIOTIC T column. It was found that teicoplanin has a higher affinity for *D*-CNPs compared to *L*-CNPs which confirms the elution order found experimentally. Chiral HPLC analysis of chiral CNPs provides a powerful toolbox to determine NP enantiopurity, stability, and recyclability. In **Chapter 3,** Chiral CNPs were applied to *S. aureus* biofilms to determine their efficacy as anti-biofilm agents. Using static biofilm models, it was found that *D*-CNPs were more effective at dispersing mature biofilms compared

to *L*-CNPs. While chiral CNPs were effective at breaking apart mature biofilms, a microdilution assay confirmed that these nanoparticles are not biocidal and can act solely as a dispersant. Conventional small molecule antibiotics are quite effective at targeting planktonic bacterial cells. Incorporating antibiotics after chiral CNP mediated biofilm dispersal would be an effective method to prevent a downstream by any released cells after biofilm disruption. Studying the interactions between chiral CNPs and PSMs, the amyloid peptides found within *S. aureus* biofilms, identified anti-biofilm activity with three modes of action. The first mode of action was chiral CNPs binding to PSMα1 and catalyzing self-assembly into rigid nanotube structures. The rigidity of these supramolecular assemblies are not native configurations typically found in the EPS and don't align with the mechanical flexibility required for maintain the integrity of the biofilm. Binding to PSMα1 also prevents co-assembly with other components in the biofilm which reduces biofilm stability. *D*-CNPs but not *L*-CNPs distorted the fibrillation of PSMα3, the PSM largely responsible for nucleating other nanofibers.[2] This offers an explanation as to why there is enantioselective dispersal of the biofilm. Lastly, chiral CNPs bind to PSMs and modulate their virulence factors that include hemolysis rate and cytokine production. In the case of hemolysis, *L*-CNPs decreased the hemolytic properties of both PSMα1 and PSMα3 more effectively than *D*-CNPs. However, *D*-CNPs was more effective at reducing PSMα3 mediated cytokine production compared to *L*-CNPs. Because *D*-CNPs were effective at biofilm dispersal but increased the hemolytic properties of both PSM peptides, it's necessary to further engineer these nanoparticles to have maximum anti-biofilm activity while mitigating negative effects to mammalian cells and tissues.

4.2 Future Work

4.2.1 Increase Resolution of Chiral CNP Separation

The resolution of the separation of chiral CNPs in **Chapter 2** could be increased by adding organic modifiers to the mobile phase or increasing the pore size of the chiral selector. The pore size within the CHIROBIOTIC T is 100 Å, which is similar to the 2-7 nm size distribution of the chiral CNPs and inhibits their diffusion deep into the stationary phase. Increasing the pore size by at least a factor of two would increase analyte retention time and resolution. The CHIROBIOTIC T2 is teicoplanin based chiral column with 200 Å pores and would be an excellent candidate to separate chiral CNPs with increased resolution. Furthermore, it would also be advantageous to investigate the separation of chiral CNP formulations from other starting materials or synthesis pathways. Chiral CNPs can be synthesized using top-down or bottom-up methods.[3] Cysteine were the most frequently used chiral precursors but other chiral molecules have been explored as well.[3] The properties of chiral CNP is dependent on the synthesis method and precursors used which could potentially change the enantiopurity and the retention times. Chiral HPLC analysis of these chiral CNP formulations would highlight their hydrolytic stability and enantiopurity.

4.2.2 Further Engineering of chiral CNP Formulations

In **Chapter 3**, *D*- cysteine derived nanoparticles were more effective at dispersing *S. aureus* but increased the hemolytic properties of both PSM peptides. Furthermore, *D*-CNPs were able to reduce PSM mediated IL-8 production while *L*-CNPs exacerbated the inflammatory response. This necessitates further engineering of chiral CNPs to have favorable biofilm dispersal capabilities while decreasing the virulence PSM peptides. This can be achieved by using different amino acids with disparate physicochemical properties. Chiral CNPs have already been synthesized from other amino acids besides cysteine such as tyrosine[4], lysine[5], arginine [6], glutamic acid[7], proline[8], and serine[9]. It is anticipated that chiral CNPs synthesized or functionalized with other amino acids would bind differently to components in the EPS and change the mechanism of action for biofilm

dispersal. Similarly, chiral CNPs with different physicochemical properties imparted by changing the amino acid functionalization would likely bind to different regions of PSM peptides and modulate their virulence factors. Synthesis and characterization of chiral CNPs from new amino acids will be time consuming. It is recommended to incorporate MD simulations to predict how chiral CNPs would bind to PSM peptides. Understanding the binding regions of the newly synthesized chiral CNPs onto PSM peptides using MD may give insight to favorable NP candidates.

4.2.3 Assess Enantioselective Biofilm Dispersal of Other Bacteria Species

In **Chapter 3**, chiral CNPs displayed enantioselective biofilm dispersal of *S. aureus* biofilms grown in PNG media. The anti-biofilm activity of chiral CNPs should be assessed in *S. aureus* biofilms grown in other media such as Luria-Bertania(LB) or glucose supplemented Tryptic soy broth (TSBg). This will highlight if the cysteine derived chiral CNPs are effective at dispersing *S.aureus* biofilms expressing different phenotypes. Besides *S. aureus* , other bacterial species such as *Escherichia Coli* (*E.coli*), *Pseudomonas Aeruginosa* (*P. aeruginosa*) , and *Bacillus subtilis* (*B.subtilis*) are also known to form biofilms.[10] The chiral CNPs used in this study should be applied to biofilms from other bacterial species to assess their broad spectrum anti-biofilm activity.These species also have functional amyloid-like peptides. *E. coli* utilizes a peptide curli to colonize inert surfaces and form biofilms. [11] *P. aeruginosa* uses amyloid fibrils (FapC) to act as adhesions and structural components within the biofilm.[12] TasA is a major protein component within *B.subtilis* biofilms that provides structural integrity.[13] It's essential to understand how chiral CNPs modulate the physiochemical properties of these amyloid peptides and their subsequent effects against mammalian hosts and tissues.

4.3 References

1. Hubbard, M. A. *et al.* Chiral chromatography and surface chirality of carbon nanoparticles. *Chirality* **34**, 1494–1502 (2022).
2. Zaman, M. & Andreasen, M. Cross-talk between individual phenol- soluble modulins in staphylococcus aureus biofilm enables rapid and efficient amyloid formation. *Elife* **9**, 1–17 (2020).
3. Döring, A., Ushakova, E. & Rogach, A. L. Chiral carbon dots: synthesis, optical properties, and emerging applications. *Light: Science & Applications 2022 11:1* **11**, 1–23 (2022).
4. Hallaji, Z., Bagheri, Z. & Ranjbar, B. One-Step Solvothermal Synthesis of Red Chiral Carbon Dots for Multioptical Detection of Water in Organic Solvents. *ACS Appl Nano Mater* **6**, 3202–3210 (2023).
5. Arad, E. *et al.* Lysine-derived carbon dots for chiral inhibition of prion peptide fibril assembly. *Adv Ther (Weinh)* **1**, 1800006 (2018).
6. Li, P. *et al.* Carbon quantum dots derived from lysine and arginine simultaneously scavenge bacteria and promote tissue repair. *Appl Mater Today* **19**, 100601 (2020).
7. Wu, X. *et al.* Fabrication of highly fluorescent graphene quantum dots using L-glutamic acid for in vitro/in vivo imaging and sensing. *J Mater Chem C Mater* **1**, 4676–4684 (2013).
8. Ostadhossein, F., Vulugundam, G., Misra, S. K., Srivastava, I. & Pan, D. Chirality inversion on the carbon dot surface via covalent surface conjugation of cyclic α-amino acid capping agents. *Bioconjug Chem* **29**, 3913–3922 (2018).

9. Zhang, M. *et al.* Chiral carbon dots derived from serine with well-defined structure and enantioselective catalytic activity. *Nano Lett* **22**, 7203–7211 (2022).

10. Muhammad, M. H. *et al.* Beyond risk: bacterial biofilms and their regulating approaches. *Front Microbiol* **11**, 928 (2020).

11. Chapman, M. R. *et al.* Role of Escherichia coli curli operons in directing amyloid fiber formation. *Science (1979)* **295**, 851–855 (2002).

12. Rouse, S. L., Matthews, S. J. & Dueholm, M. S. Ecology and biogenesis of functional amyloids in Pseudomonas. *J Mol Biol* **430**, 3685–3695 (2018).

13. Romero, D., Aguilar, C., Losick, R. & Kolter, R. Amyloid fibers provide structural integrity to Bacillus subtilis biofilms. *Proceedings of the National Academy of Sciences* **107**, 2230–2234 (2010).

Appendices

Appendix A: Chiral Chromatography and Surface Chirality of Carbon Nanoparticles Supplemental Information

This appendix contains additional information for **Chapter 2** from the publication: Hubbard, MA, Luyet, C, Kumar, P, et al. Chiral chromatography and surface chirality of carbon nanoparticles. *Chirality*. 2022; 34(12): 1494- 1502.

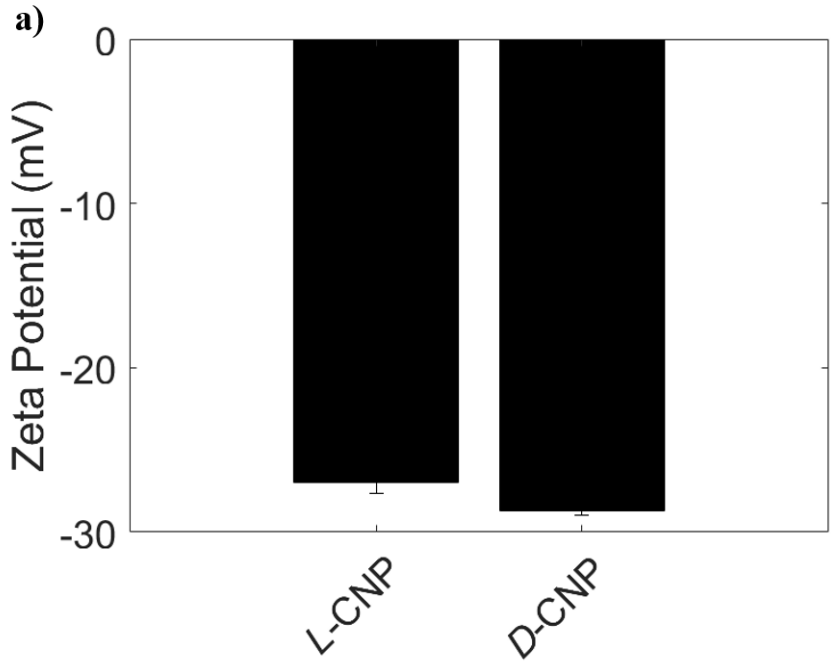

Figure A.1: Zeta-potential of chiral CNPs.

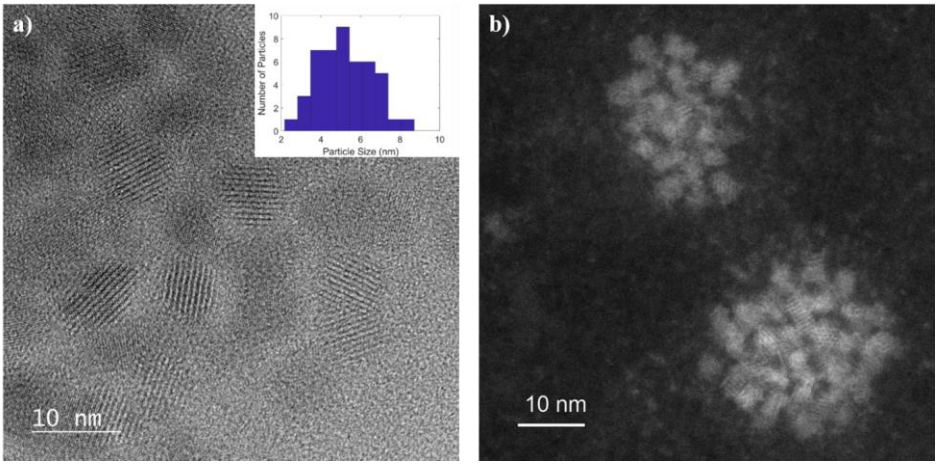

Figure A.2: a) TEM image of *D*-CNPs with histogram inlay b) STEM image of *D*-CNPs.

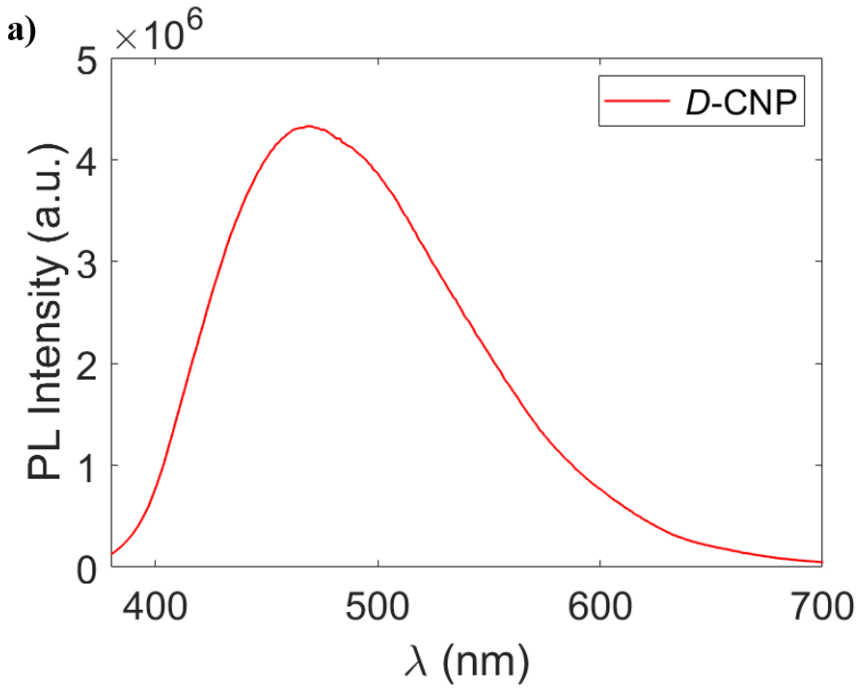

Figure A.3: Emission spectra of *D*-CNPs after separation.

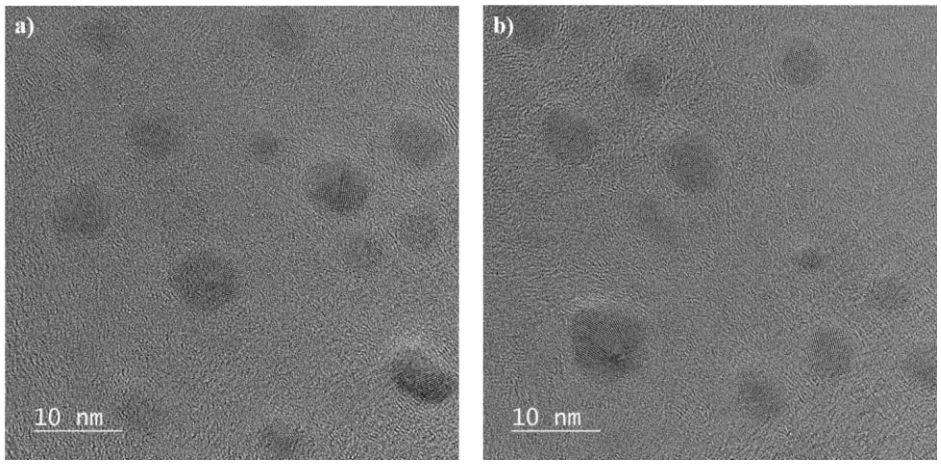

Figure A.4: TEM images of *D*-CNPs after separation.

Appendix B: Anti-Biofilm Activity of Chiral Carbon Nanoparticles Supplemental Information

This appendix contains additional information for **Chapter 3** from the publication: Hubbard, MA, Luyet, C, Kumar, P, et al. Chiral chromatography and surface chirality of carbon nanoparticles. *Chirality*. 2022; 34(12): 1494- 1502.

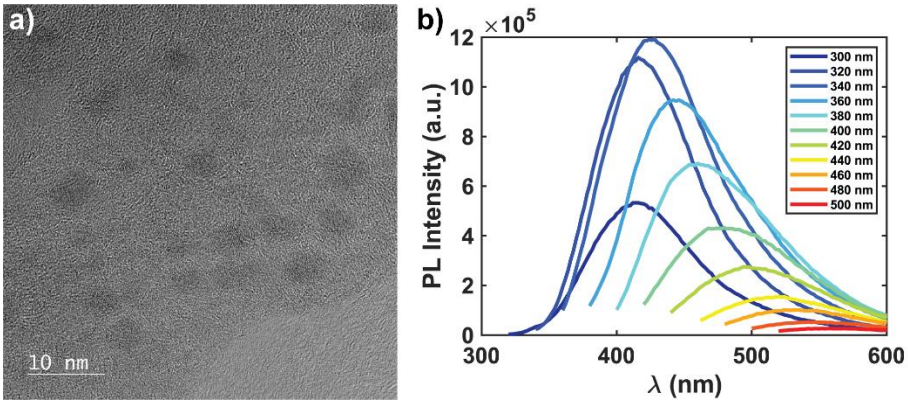

Figure B.1: Structural and spectroscopic characterization of CNPs. A) TEM image and b) emission spectra of *D*-CNPs

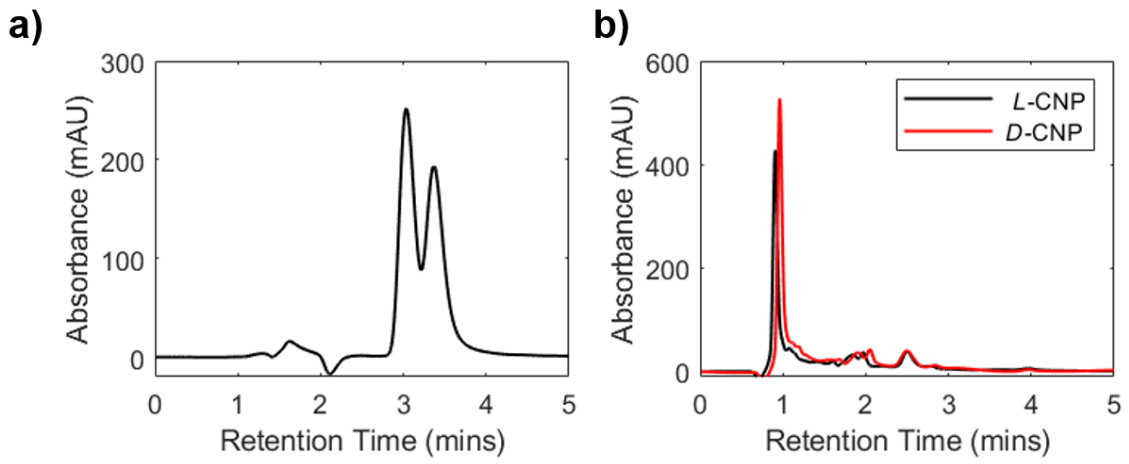

Figure B.2: Chromatographic separation of a) Racemic cysteine b) chiral CNP treated biofilm supernatant. Figure adapted with permission from REF [1]. ©2022 Chirality

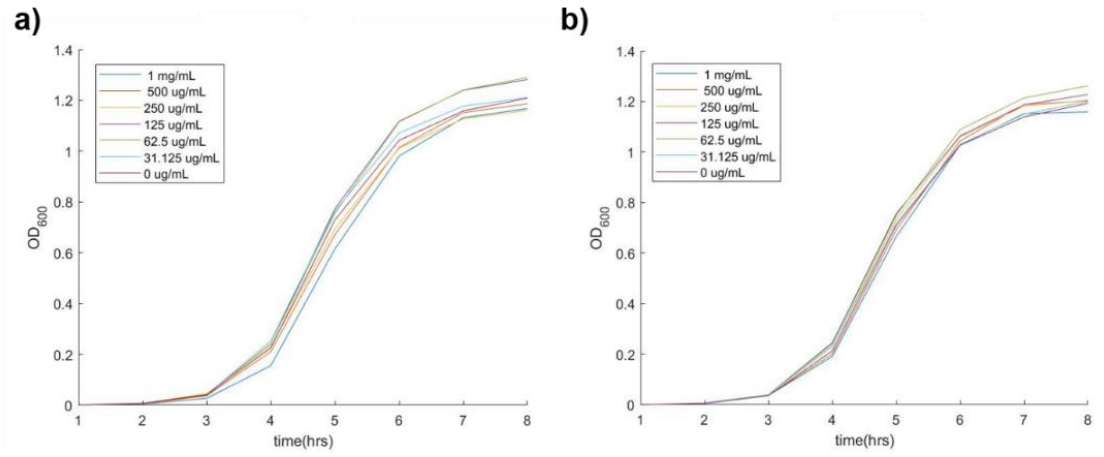

Figure B.3: Minimum inhibitory concentrations of a) *L*-CNPs and b) *D*-CNPs against planktonic S. aureus cells.

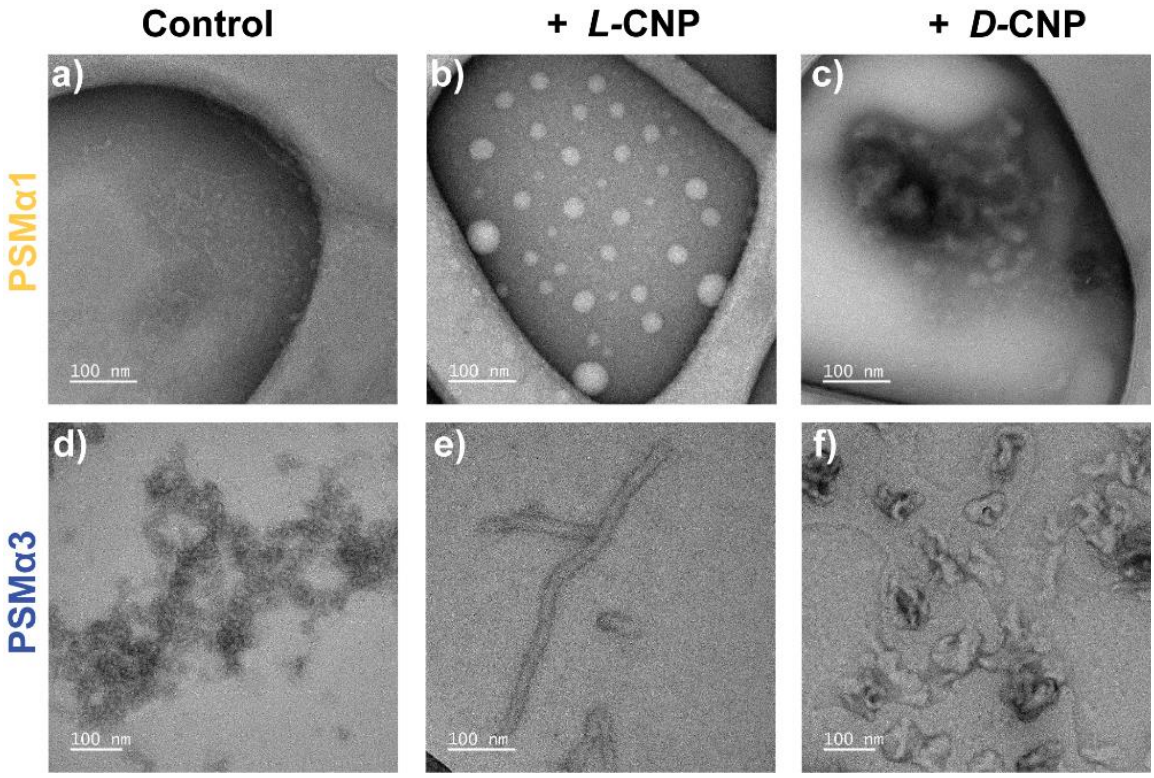

Figure B.4: TEM images at t = 0 hrs for a) PSMα1 b) PSMα1 + *L*-CNPs c) PSMα1 + *D*-CNPs d) PSMα3 e) PSMα3 + *L*-CNPs f) b) PSMα3 + *D*-CNP

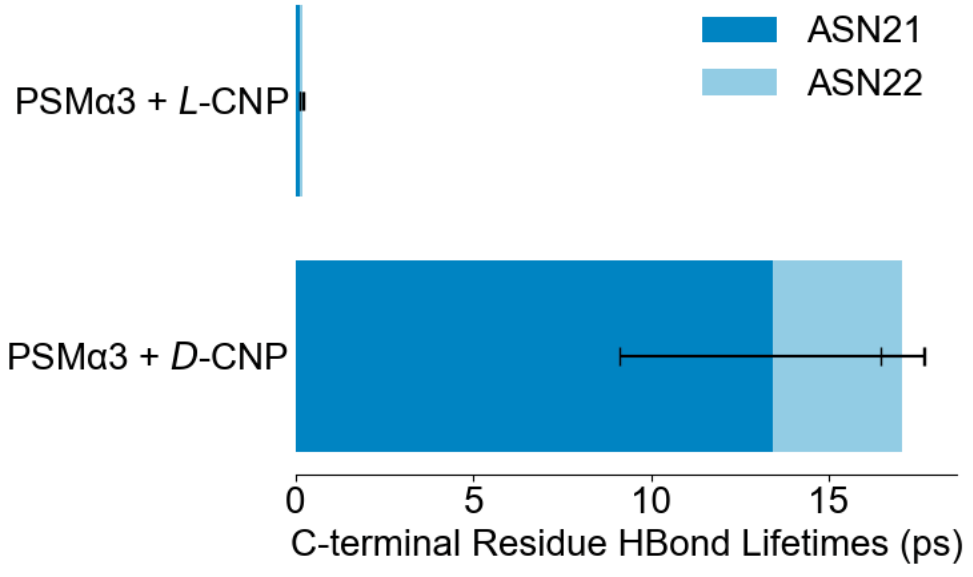

Figure B.5: PSMα3's ASN21 and ASN22 Prefer D-CNP. Data is collected from ***group*** simulations. Error bars are standard errors of the mean, taken at 5ns intervals of the trajectory.

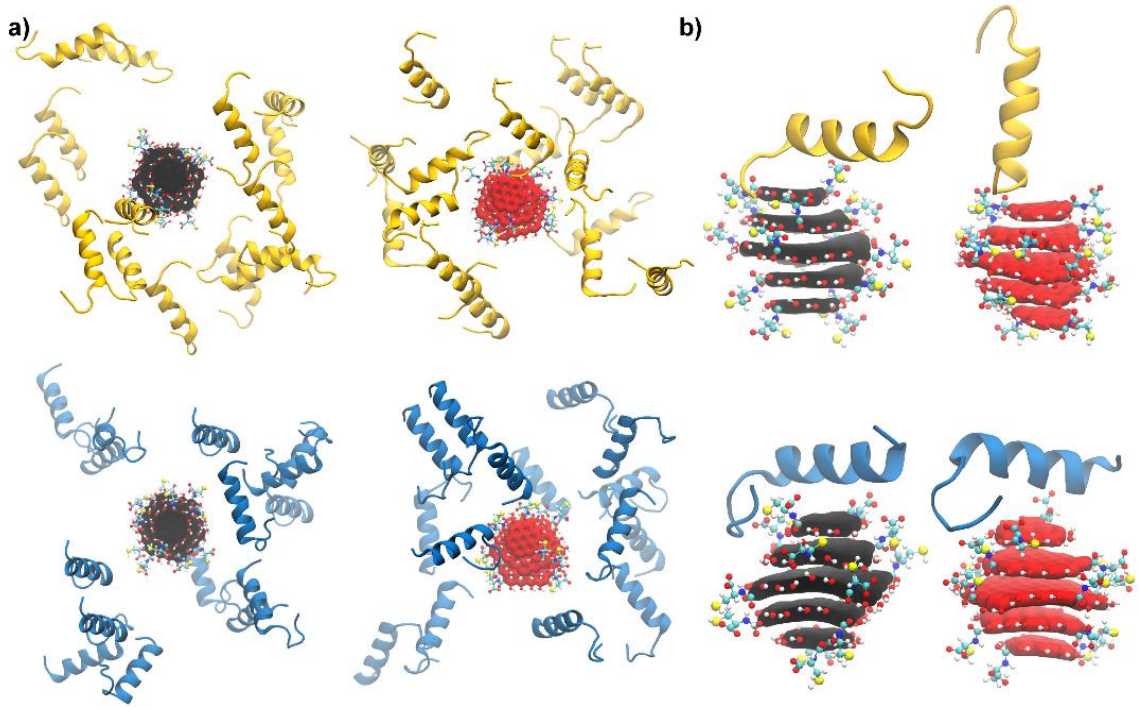

Figure B.6: Example of initial configurations for (a) a group (15) of PSMs surrounding 1 CNP and (b) a single PSM interacting with 1 CNP. *D*-CNP is shown in red, *L*-CNP in black, PSMα3 in blue and PSMα1 in yellow. Water and ions are hidden for clarity.

References

1. Hubbard, M. A. *et al.* Chiral chromatography and surface chirality of carbon nanoparticles. *Chirality* **34**, 1494–1502 (2022)